

Unravelling the origins of anomalous diffusion: from molecules to migrating storks

Ohad Vilk^{1,2}, Erez Aghion³, Tal Avgar⁴, Carsten Beta⁵, Oliver Nagel⁵,
Adal Sabri⁶, Raphael Sarfati⁷, Daniel K. Schwartz⁷, Matthias Weiss⁶,
Diego Krapf⁸, Ran Nathan², Ralf Metzler⁵, Michael Assaf^{1,5*}

¹Racah Institute of Physics, The Hebrew University of Jerusalem, Jerusalem, Israel

²Movement Ecology Lab, Department of Ecology, Evolution and Behavior,
Alexander Silberman Institute of Life Sciences, Faculty of Science,
The Hebrew University of Jerusalem, Jerusalem, Israel

³Departments of Physics and Chemistry, University of Massachusetts Boston,
MA 02125, USA

⁴Wildlife Space-Use Ecology Lab, Department of Wildland Resources and Ecology Center,
Utah State University, Logan, UT 84332, USA

⁵Institute of Physics and Astronomy, University of Potsdam, Potsdam 14476, Germany

⁶Experimental Physics I, University of Bayreuth, D-95440 Bayreuth, Germany

⁷Department of Chemical and Biological Engineering, University of Colorado Boulder,
Boulder, CO 80309, USA

⁸Department of Electrical and Computer Engineering, and School of Biomedical Engineering,
Colorado State University, Fort Collins, CO 80523, USA

*To whom correspondence should be addressed; E-mail: michael.assaf@mail.huji.ac.il

Anomalous diffusion or, more generally, anomalous transport, with nonlinear dependence of the mean-squared displacement on the measurement time, is ubiquitous in nature. It has been observed in processes ranging from microscopic movement of molecules to macroscopic, large-scale paths of migrating birds. Using data from multiple empirical systems, spanning 12 orders of magnitude in length and 8 orders of magnitude in time, we employ a method to detect the individual underlying origins of anomalous diffusion and transport in the data. This method decomposes anomalous transport into three primary effects: long-range correlations (“Joseph effect”), fat-tailed probability density of increments (“Noah effect”), and non-stationarity (“Moses effect”). We show that such a decomposition of real-life data allows to infer nontrivial behavioral predictions, and to resolve open questions in the fields of single particle cell tracking and movement ecology.

Introduction

Normal diffusion or transport processes obey the Gaussian central limit theorem (CLT) and are ergodic; *i.e.*, mean values of various observables in the system do not depend on the averaging method. The CLT states that, if a random time series $x(t)$ is the sum of random variables which are (i) identically distributed (with a stationary distribution), (ii) have a finite variance, and (iii) are independent, the probability density function (PDF) $P(x, t)$ of x at time t has a Gaussian shape (Supplemental Sec. S1.1). The mean-squared displacement (MSD) then satisfies $\langle x^2(t) \rangle \propto t$ at long times, where $\langle \cdot \rangle$ denotes ensemble averaging (EA). Yet, advances in high fidelity methods for single-particle tracking (1, 2) and detailed data of animal paths (3, 4) show that many natural processes are in fact *anomalous*, as they violate (some of) the CLT’s conditions (5). Condition (i) can be violated, *e.g.*,

when the measured trajectories are confined for increasingly long periods in certain spatial regions, hindering their expansion. Condition (ii) can be violated, *e.g.*, in financial time series, where large fluctuations are highly probable. Condition (iii) can be violated, *e.g.*, for biased or correlated motion. Such violations typically yield $\langle x^2(t) \rangle \propto t^{2H}$, with the Hurst exponent being $H \neq 1/2$.

Given an empirical time series displaying anomalous transport, the ability to distinguish between the various violations of the CLT is crucial, *e.g.*, to determine the system's expansion rate (6, 7), rare event statistics (8, 9), method of averaging (10–12), to infer features in the diffusion medium (13–16) and elucidate the underlying microscopic process. Indeed, this characterization is a major challenge in various fields including single particle tracking and movement ecology (17–19), and much effort is made to develop techniques to tackle it; see, *e.g.*, Refs. (20–23).

Here, based on positional (tracking) data, we employ a specialized three-effect decomposition method (24, 25) to disentangle the effects leading to anomalous transport, without making prior assumptions on the underlying model governing the dynamics. By analysing three independent properties of the time series presented below, we determine whether the measured diffusion is anomalous due to violation of condition (i), (ii) and/or (iii) above. To establish the broad applicability of the technique, we study empirical data sets that range over 12 orders of magnitude in length (10^{-6} – 10^6 m), and 8 orders of magnitude in time (10^{-3} – 10^5 s). Beyond empirical data, we also present results of numerical simulations of random walk models, which have been previously proposed to describe some of these systems. Notably, applying this method provides important insight into key open questions in various scientific fields, as detailed below. Thus, we aim at promoting this method as a common practice for future empirical studies of anomalous transport.

Consider a stochastic process $\mathbf{x}(t)$ in $d \geq 1$ dimensions (vectors are denoted in bold font). For instance, $\mathbf{x}(t)$ can represent a time-series of the distance traveled by a bird (from its nest) in the course

of one day, as function of time, where one can always set $\mathbf{x}(0) = \mathbf{0}$. The process $\mathbf{x}(t)$ can be described by a discrete sum of random increments, $\mathbf{x}(t) = \sum_{j=1}^N \delta \mathbf{x}_j$, where $\delta \mathbf{x}_j \equiv \mathbf{x}(j\Delta) - \mathbf{x}([j-1]\Delta)$ and $N = t/\Delta$, while $0 < \Delta \ll t$ is an arbitrary time increment. Moreover, $\mathbf{v}_j \equiv \delta \mathbf{x}_j/\Delta$ is the average velocity vector in the j th increment, and the *velocity* PDF, $P(|\mathbf{v}|, t)$, is the distribution of its absolute value. To distinguish between the above three different ways of violating the CLT in an empirical time series, we compute the corresponding increments of $\mathbf{x}(t)$ and analyze their size-statistics (24, 25), as shown in Fig. 1. We compute three numerical values that describe the temporal scaling of three observables: (i) mean absolute velocity $\langle |\mathbf{v}| \rangle$, (ii) mean-squared velocity $\langle \mathbf{v}^2 \rangle$, and (iii) ensemble-averaged time-averaged MSD (TAMSD) $\langle \overline{\delta^2(t, s)} \rangle$, as detailed below (26).

Non-stationarity. For a time-varying velocity PDF, condition (i) of the CLT is violated due to the “**Moses effect**” (25–27). This is quantified by the exponent M , measured via the relation

$$\langle \overline{|\mathbf{v}|(t)} \rangle = \left\langle \frac{1}{t-\Delta} \sum_{j=1}^{t/\Delta} |\mathbf{v}_j| \right\rangle \propto t^{M-1/2}, \quad (1)$$

where the overline indicates time averaging (TA). The Moses effect occurs when $M \neq 1/2$, implying either accelerating ($M > 1/2$) or decelerating ($M < 1/2$) dynamics, *e.g.*, due to aging; the latter means that the process can be slowed down randomly for increasingly long times, and therefore the observed dynamics may seem different depending on the time of measurement. A key consequence of this effect is *weak-ergodicity breaking* (10, 11, 28), as ergodicity requires stationarity. In Fig. 2a we plot an example of a simulated non-stationary accelerating process; below this panel we list the different regimes of M and their physical interpretation.

Extreme events. For a growing in time $\langle \mathbf{v}^2 \rangle$ (given a finite ensemble) condition (ii) of the CLT is violated due to the “**Noah effect**” (24), quantified by the latent exponent L :

$$\langle \overline{\mathbf{v}^2(t)} \rangle \equiv \left\langle \frac{1}{t-\Delta} \sum_{j=1}^{t/\Delta} \mathbf{v}_j^2 \right\rangle \propto t^{2L+2M-2}. \quad (2)$$

By definition $L \geq 1/2$ (24). If, for a stationary velocity PDF with $M = 1/2$, in addition $L = 1/2$, $\langle \mathbf{v}^2 \rangle$ is constant. Yet, if $L > 1/2$, its value will grow in time, even though $M = 1/2$. As opposed to $\langle |\mathbf{v}| \rangle$, which is a measure of the typical fluctuations in a time series, $\langle \mathbf{v}^2 \rangle$ in anomalous diffusion is controlled by the tails of the velocity PDF. In the absence of extreme events $\langle \mathbf{v}^2 \rangle \propto t^{2M-1}$. A deviation from this scaling, quantified by L (for any M), is a proxy for detecting extreme rare events dominating the path with increasing probability as time evolves. The resulting expansion rate of the diffusing packet may thus be faster than linear. This occurs, *e.g.*, in Lévy flights (6, 25, 29), where the noise is scale-free. An example for a process with rare extreme events is given in Fig. 2b, where below this panel we list the different regimes of L and their physical interpretation.

Temporal autocorrelations. Violation of condition (iii) of the CLT occurs via the “**Joseph effect**” (24, 25, 30, 31), quantified by the exponent $0 < J \leq 1$. Formally, J is defined via the velocity autocorrelation function (Supplemental Sec. S1.2), which can have a positive or negative sign, describing a positively- (persistent) or anti-correlated (anti-persistent) process, respectively. While J can be measured in various ways (25–27), here we use the TAMSD (26, 27, 32) (Supplemental Sec. S1.2):

$$\left\langle \overline{\delta^2(s, t)} \right\rangle = \left\langle \frac{1}{t-s} \int_0^{t-s} [\mathbf{x}(t'+s) - \mathbf{x}(t')]^2 dt' \right\rangle \propto t^{2L+2M-2} s^{2J}. \quad (3)$$

For long-ranged temporal correlations (decaying very slowly in time) one has $J \neq 1/2$, thus violating the CLT, which requires only short-ranged temporal correlations. Another option is temporal anti-correlations (24). The driving mechanism behind this effect can be, *e.g.*, biased movement, diffusion in confined space, or long-range memory. An example for a process with long-range memory is given in Fig. 2c, where below this panel we list the different regimes of J and their physical interpretation.

The above definitions yield a fundamental **summation relation** between M , L , J and H (25–27):

$$H = J + L + M - 1, \quad (4)$$

This relation, connecting these three effects, is central for all the results presented below, and is confirmed from analysis of a large variety of empirical systems. An observed process resembles simple Brownian motion, if $L = M = J = H = 1/2$. Note, that the underlying assumption for this method is that the scaling relations [Eqs. (1-3)] are valid at least locally over some finite time interval; here, the summation rule means that the above three effects are exhaustive for violating the CLT.

Results

We detect the origins of anomalous diffusion in 7 different systems, comprised of 16 empirical setups: rhodamine molecules diffusing within water nanofilms with varying relative humidity (33); tracer particles (quantum dots) in the cytoplasm of untreated and treated mammalian cells (21); flat amoeba cells (*Dictyostelium discoideum*) diffusing on a surface (34); harvester ants (*Messor arenarius*) embarking on foraging trips (35); a single black-winged kite (*Elanus caeruleus*) during commuting and area-restricted searches (12); a single white stork (*Ciconia ciconia*) (36) clustered according to seasonality; and a single Eurasian griffon vulture (*Gyps fulvus*, Hablizl 1783) (37). Each setup is represented by an ensemble of time series, for which we obtain statistics in terms of the above quantities. For mathematical details and error analysis, see Methods and Supplemental Sec. S1.3.

In Table 1, we summarize the scaling exponents J, L, M , measured for all systems and experiments, along with the predicted value of H based on Eq. (4), denoted by H_p . Remarkably, for all data sets, we find good agreement between H determined from $\langle x^2(t) \rangle$ and H_p , with a relative error $\leq 10\%$, thus confirming the validity of Eq. (4) in the empirical data. In most of the studied data sets anomalous diffusion is primarily caused by the *Joseph and Moses effects*; the *Noah effect* was only observed for the stork and searching kite. We now list the exponents we found for each empirical setup, suggest *plausible* models, and discuss various implications of our findings (in the main text

we present figures with the complete analysis for three prototypical examples: amoebas, stork and vulture; for the rest see Supplemental Sec. S2).

Rhodamine molecules. For the fluorescent rhodamine molecules, the primary effect was found to be a Joseph effect (anti-correlation), leading to subdiffusion (Supplemental Sec. S2.1), where the effect is strongest at the lowest relative humidity of 30% ($J = 0.09$), see Table 1. This effect can be interpreted as viscoelasticity in the water film, possibly due to significant persistent ordering between H₂O molecules induced by strong coupling to the silicate or silanol groups of the silica surface. As humidity increases and water nanofilms grow in thickness, molecular ordering becomes more random and less persistent, and the water film becomes more viscous farther from the silica surface, resulting in a decrease of J . A fractional Brownian motion (FBM)-like process (7) can be used to model the movement of these particles, exhibiting confined diffusion. Yet, contrary to “pure” FBM, we also observed a negative (although weak) Moses effect at short times for any humidity, suggesting a combined effect of FBM with scaled Brownian motion (SBM) or continuous-time random walk (CTRW) (7), see simulations in Table 1. The subordination of FBM by a CTRW is also suggested by (33) and is consistent with the physical mechanisms of intermittent diffusion at solid/liquid interfaces, whereby a molecule desorbs from the surface, diffuses in the viscous phase, and re-adsorbs (38, 39).

Tracer particles in mammalian cells.

In both treated and untreated cells, the statistics display two temporal regimes (Supplemental Sec. S2.2). In the first regime ($t < 5$ s and $t < 2$ s for the treated and untreated cells, respectively) the dynamics are anti-correlated, with a weak negative Moses effect and no Noah effect. Together, these effects lead to significant subdiffusion with $H = 0.31$. In contrast, in the second regime ($t > 5$ s and $t > 2$ s) the Joseph effect is measurably different between the treated and untreated cells. While

for untreated cells the dynamics are correlated and hence superdiffusive, for the treated cells they are not correlated, and a Moses effect leads to subdiffusion. Our results are consistent with those of (21) (Supplemental Sec. S2.2). The elevated values for J in the second regime suggest that on time scales of a few seconds, particles are being kicked by an active ambient noise that arises by cytoskeleton-associated transport processes in the surrounding (40–42). This notion is in line with a reduction of J when breaking down actin filaments which prevents the contribution of slow active processes linked to cell reshaping and migration. The presence of a weak Moses effect at all time scales is most likely due to the intermittent mobility change found for these tracers, as they transiently adsorb to and desorb from the cell’s vast endomembrane system (21). Notably, in temporal regimes with measurable Joseph and Moses effects, the system can be modeled, *e.g.*, by scaled FBM (SFBM), see Table 1. Yet, as the Moses effect is very weak, and as particles are non-specifically bound to a dynamic endoplasmic reticulum (21), FBM cannot be discarded entirely.

Amoebas. In Fig. 3 for the tracked amoebas, we depict the analysis workflow that we repeat for all empirical data sets. Here, the statistics display two temporal regimes, with different scaling exponents, which indicates a change in the amoeba dynamics at intermediate times. For $1 < t < 6$ min the dynamics are positively correlated ($J = 0.61$), which is the dominant effect leading to superdiffusion ($H > 0.5$), and exhibit a weak Moses effect and no Noah effect. In contrast, for $10 < t < 100$ min the dynamics are not correlated; rather, a negative Moses effect, entailing statistical slowing down, leads to subdiffusion ($H < 0.5$). Thus, the primary cause for anomalous diffusion differs between the regimes. As a result, we conjecture that in the first regime the underlying process is FBM with positive correlations, while in the second regime it resembles SBM which results in a Moses effect, in agreement with the analysis performed in Ref. (34). A consistency check of the observed exponents with concrete stochastic simulations is given in Table 1. Importantly, while the extracted exponents

do not allow unique model identification, they provide important insights into the detailed dynamics of the observed motion.

Ants. For the harvester ants, we find (Supplemental Sec. S2.3) that for $10 < t < 100$ s the movement is strongly correlated ($J = 0.88$) with a small positive Moses effect, leading to superdiffusion. In this regime the ants are behaviorally persistent, primarily commuting between the nest and food sources in relatively straight lines, leading to biased-correlated movement. In contrast, for $100 < t < 400$ s the movement is significantly less correlated and non-stationary ($J = 0.59$ and $M = 0.35$). Both the positive Joseph and negative Moses effects likely reflect behavioral shifts between commuting (superdiffusive) and searching or handling seeds (diffusive or subdiffusive). While the Hurst exponent may suggest (almost) Brownian diffusion at these times, this is not the case; rather we measure $H = 0.47$ due to a nontrivial coupling of the Joseph and Moses effects, likely common in many central-place foraging movements.

Kite. We separately analyse ensembles of commuting and search flights. During commuting, for $t < 3$ min and $t > 3$ min the dynamics are positively correlated ($J = 0.87$ and $J = 0.80$ respectively), leading to superdiffusion (Supplemental Sec. S2.4.1). Here, the Moses and Noah effects are negligible, and since the MSD and TAMSD scale similarly with time, the process is ergodic (7). Indeed, the most efficient way to commute among patches is to fly in a straight line directed towards the target (strong positive Joseph effect). These commuting flights are taken in a steady cruising speed (no Moses effect) and also without extreme jumps (no Noah effect), suggesting lack of support for the Lévy foraging hypothesis (43–45). During searches, the statistics display a single regime (Supplemental Sec. S2.4.2). Here the dynamics are anti-correlated with $J = 0.24$ and there are measurable Moses and Noah effects, $M = 0.22$ and $L = 0.59$. Kites search locally in a spatially confined manner to avoid departure from a patch (negative Joseph effect), with relatively long stops in particular

locations (negative Moses effect) and also rare relatively-long jumps between these locations (Noah effect). Our results support the findings of (12) that the kite's searches can be modeled as a bounded CTRW, see Table 1.

Stork. Daily paths are clustered into four subsets, according to the time of year: June-July, August-September, October-January, March-April, respectively corresponding to four periods in a life cycle of the bird: breeding, fall migration, wintering, and spring migration (36). Using this simple clustering, we aim to capture important features of the stork's life history (Fig. 4).

During *breeding* (June-July), we observe subdiffusive motion at all times ($H < 0.5$). For $t < 2$ h and $t > 2$ h subdiffusion is caused by a strong negative Moses effect coupled to a strong Noah effect ($M = -0.24, L = 0.88$), and anti-correlated movement ($J = 0.18$), respectively. In hot days, breeding storks fly early in the morning to forage in neighboring fields (> 5 km away (36)), but remain longer times in the nest during the hottest hours to thermoregulate the eggs or nestlings. Flights occur earlier in the morning, and are much faster and less frequent than foraging walks or stops in the nest, with relatively long waiting times, explaining the strong Noah and negative Moses effects in the first regime. The tendency to return to the nest during the remaining parts of the day explains the strong negative Joseph effect appearing in the second regime, while the disappearance of the Moses and Noah effects in this regime may be since the waiting times distribution is no longer scale free. Notably, the coupling of the Moses and Noah effects was also found, *e.g.*, in CTRW simulations, see Table 1 and Methods. In contrast, the observed exponents in the second regime may emanate from movement within a (self determined) bounded domain, or from FBM, see Table 1. Both long waiting times and bounded movement are supported by the movement paths (Fig. 4A) and may be generated by the spatio-temporal constraints of a breeding animal.

During *wintering* (October-January), the movement patterns are superdiffusive in two regimes

($H = 0.74$ and $H = 0.80$). Here, for $t < 2$ h and $t > 2$ h superdiffusivity is primarily caused by long-range correlations ($J = 0.78$), and strong positive Moses effect ($M = 0.65$), respectively. While the Joseph effect *decreases* between the two regimes, their H values are similar due to a transition between negative and positive Moses effect ($M = 0.25$ to $M = 0.65$). Thus, the movement is evidently nonergodic. The similarity of H in both regimes stresses the significance of performing the full three-effect decomposition in anomalous data, rather than only looking at the MSD scaling. During winter, movement patterns of storks reflect a mixture between their moves during breeding and migration. On the one hand, during winter they move much longer distances than during breeding, including long migration-like directional flights to distant wintering sites (Fig. 4B) that give rise to a positive Joseph effect. On the other hand, wintering storks resemble breeding ones in their confined movement for days or weeks and roosting in a central place from which they fly to their foraging sites early in the morning. Here, they search for food mostly by walking, giving rise to Noah and negative Moses effects in the first regime (as in breeding). Storks also tend to be less mobile during mid day (as in breeding) but resume foraging in the afternoon (unlike breeding), explaining the lack of Noah effect and the shift to a positive Moses effect in the second regime. Notably, the Noah effect ($L > 1/2$), appearing for both breeding and wintering, may stem from the fact that various aspects of the stork's daily routine remain constant, despite the underlying seasonal behavior. Throughout the year the stork can move via walking at a range of velocities (46), short-term flights (mostly within a food patch) and long-term commuting (*e.g.*, from the nest to foraging ground). Thus, flights may appear as a heavy tail compared to the bulk, comprised mainly of short-scale walks. This is in striking contrast to the lack of a Noah effect for the vulture which travels only via flights, see below.

During fall and spring *migrations* (August-September and March-April) the statistics are similar: for $t < 2$ h and $t > 2$ h we find a strongly correlated movement with a small positive Noah effect,

and a strong positive Moses effect with no Noah effect, respectively. Migrating storks take highly directional flights from the breeding to wintering grounds during fall (Fig. 4C), and vice versa during spring (Fig. 4D), giving rise to a strong positive Joseph effect in both cases. They roost in stopover sites during night and tend to depart in late morning, when soaring conditions improve, facilitating faster flights at lower energy costs (47). This explains the positive Moses effect in the second regime. Here, a plausible model for movement is a biased CTRW (28), see Table 1.

Vulture. For the daily paths of the vulture (Fig. 5), for $t < 2$ h the movement is superdiffusive and ergodic (7, 48), as it is positively correlated ($J = 0.75$), with a weak Moses and no Noah effects; for $t > 2$ h a positive Moses effect ($J = 0.57$ and $M = 0.63$) leads to superdiffusive behavior and ergodicity breaking. Vultures fly relatively straight away from, or back to, their roost, and to search for occasional carcasses or those randomly (in time) supplied in a few dozens of feeding stations scattered throughout their foraging area in Israel, explaining the positive Joseph effect. Despite the occurrence of very long flights (Fig. 5), the Lévy foraging hypothesis is not supported for this species (no Noah effect), in accord with (45). Vultures tend to move faster towards a known target compared to the preceding search phase (37), and like migrating storks, they fly faster when soaring conditions improve (from late morning to early afternoon), altogether explaining the positive Moses effect.

Summary and discussion

We have demonstrated the wide applicability of a general method (24, 25) to unravel the origins of anomalous transport in empirical time series in chemistry, biology and ecology, over multiple spatio-temporal scales. Using positional time series, almost free from prior assumptions and with little-to-none auxiliary information, the method decomposes the Hurst exponent into three components: non-stationarity, fat-tailed distributions, and long-range correlations. The decomposition is manifested by

a summation rule, and is verified for all analyzed data sets.

Our analysis provides insight into the inherent correlations and physical differences between the analysed scaling exponents, that are expected in empirical data, as anomalous transport can be generally due to multiple effects (25–27). In Fig. 6 we study these correlations by plotting the relation between various combinations of the exponents J , L , M and H , using the values in Table 1. We find that J and H are strongly correlated ($J \sim 0.69H$); yet, J alone is not sufficient to predict the value of H . Rather, we find that $J + M + L - 1 \simeq 0.94H$ (Supplemental Sec. S1.2). The fact that J is generally smaller than H indicates that, while some anomalous processes are ergodic ($J \simeq H$), many are not. Thus, the ergodicity assumption may lead to erroneous analyses (48). Figure 6 also reveals that M and L are anticorrelated, while M and J are correlated, suggesting inherent relations between the Moses and Noah, and Moses and Joseph effects. In contrast, L and H are not correlated, suggesting that Lévy-flight-like processes (where L gives the dominant effect) are rarer. Rather, we find that anomalous diffusion is mostly due to temporal auto-correlations and non-stationarity.

Although no unique model can be assigned to a system based only on its given set of exponents, our framework plays a key role as a decision tree allowing to identify a model class, and rule out inappropriate models (49). For example, in Lévy flights as defined in Ref. (25), one expects $L > 1/2$ and $M = J = 0.5$, which was not found for any of the data sets we analyzed. Instead, the correlations between M and L found in the data also occur, *e.g.*, in CTRW, see Table 1, suggesting CTRW to be a more plausible model here. Notably, this example gives key insight into an open question in ecology, of whether, for a given data set, an animal follows a Lévy flight (Noah effect), or a combination of a biased-correlated random walk (Joseph effect) and scaled motion (Moses effect) (44, 50). Moreover, when the Joseph effect is present, specific empirical input is needed to distinguish between biased and correlated processes. For example, within its large yet spatially confined foraging range, the vulture

searches for carcasses in circular-like paths, whereas rare long-range forays outside its home range are highly directional (37, 45) (Fig. 5), suggesting that Joseph effect represents, respectively, correlated vs. biased movement.

Three restrictions can strongly impact our analysis. First, as processes with a Moses effect are generally non-ergodic and can display aging (7), the values of M (and also L , see Fig. 6) can change depending on the relative time lag between the process's initiation time and the initial measurement time. Thus, minimizing this time lag is desirable to reflect the properties of the measured phenomenon (Supplemental Sec. S3). Second, nonergodic processes are sensitive to the ensemble size, even for comparably large ensembles. As nonergodic systems display large variability across different realizations (7), removing even a few can strongly affect the underlying statistics (48). Third, results may be sensitive to the sampling frequency, and in general, it is desirable to have a sampling frequency higher than the natural frequency of the process. Notably, when applying power-law fits to data, there are various statistical methods that provide confidence about the results. While J , L and M may be sensitive to the above restrictions and method of fitting, we checked that they vary in such a way to maintain the validity of the summation relation. Regardless, in future theoretical work, it would be useful to generalize the theory [Eqs. (1-3)], to the case of non-pure power laws.

Importantly, based on the evidence and agreement of our analysis, along 12 orders of magnitude in space, we foresee that this method will provide useful results also in other fields such as cell biology and climate change, where anomalous time series are also common.

Materials and methods

Here we provide the technical details of the data analysis in the various systems we studied, and the simulations. Furthermore, in the Supplemental Information we add python codes for numerically

obtaining the four exponents L , M , J and H from empirical data.

Empirical systems

Rhodamine molecules

A solution of rhodamine 6G molecules was deposited onto a cleaned borosilicate glass coverslip, then dried in a vacuum chamber for 30 min. The dry surface was then exposed to various degrees of ambient relative humidity between 30% and 100%, which resulted in the equilibrium condensation of water nanofilms of a few (1 to 8) molecular layers, with thicknesses that increased systematically with increasing humidity. Individual rhodamine molecules were recorded using a total internal reflection fluorescence (TIRF) microscope (532 nm laser excitation) with image acquisition times of 50 ms. Tracking (object localization and trajectory linking) was performed using custom MATLAB code. Approximately 10^4 trajectories were captured for each condition; see Ref. (33) for details.

Tracer particles in the cytoplasm of mammalian cells

Tracer particles (Qdot 655 ITK Carboxyl core (CdSe)-shell (ZnS), ThermoFisher, Waltham, MA) were incorporated into HeLa (human cervical cancer) cells by bead loading, followed by a relaxation time of 1 h before imaging. In preparation for this procedure, cells were plated 36-48 h prior to bead loading on 35 mm diameter ΔT dishes (Biotech, Butler, PA) for temperature control, coated with 0.5% matrigel matrix (Corning Life Sciences, NY) for improved adhesion. Depolymerization of actin filaments was induced by adding 200 nM latrunculin A to the medium directly after bead loading. Images were acquired with an EMCCD camera at 10 frames/s on a custom-built microscope equipped with an Olympus PlanApo 100 \times NA1.45 objective, a CRISP ASI autofocus system, and a MicAO 3DSR adaptive optics system (Imagine Optic, Orsay, France) to correct optical aberrations. Quantum dots were excited at 561 nm under continuous illumination and trajectories were extracted from image

stacks with FIJI/TrackMate. Removing immobile tracks, this approach eventually yielded large data sets from which a random selection of $M = 1000$ ($M = 200$) tracks with $N = 100$ ($N = 500$) positions were used for untreated (latrunculin-treated) cells. For further details, see supplemental material of (21).

Motile amoeba

Tracking of motile cells was performed with the social amoeba *Dictyostelium discoideum*, using AX2 wild-type cells that were cultivated in HL5 medium on polystyrene Petri dishes or in shaken suspension. Prior to imaging, cells were washed, the HL5 medium was renewed, and cells were placed on a plastic Petri dish at an average density between 1 and 2×10^4 cells per cm^2 and allowed to attach to the surface for 30 minutes. Cells were then recorded for 6 hours with a bright-field microscope at a frame rate of 0.05 Hz. To track the cells, images were segmented and the centers of mass of regions corresponding to the cells were calculated and connected from one frame to the next by nearest neighbor particle tracking. Segmentation and tracking were performed with a custom-made MATLAB algorithm (MathWorks, Ismaning, Germany) using well-established particle-tracking methods. If cells were lost during the tracking procedure because they left the field of view, collided with a neighboring cell, or divided, the recorded track ended, and a new trajectory was started once a new cell could be detected in the field of view. Only trajectories with over 60 time steps were used in the analysis; See Ref. (34) for details.

Harvester ants

Movement paths of individual harvester ants (*M. arenarius*; a solitary foraging species) were mapped in 2005 as part of research conducted in "Sayeret-Shaked" park, North-Western Negev desert, Israel (see (35) for further details). Individual ants, each from a different colony, were marked with colored

fluorescent powder and then tracked by placing numbered pins at their positions every 10 s (with minimal interference to the ant's behavior). Route mapping started once the ant departed the nest (after entering it at least once since being marked) and ended after two consecutive foraging trips (whether successful or not). Pins were then mapped at 1 cm resolution using measurement tapes and a costume-built wooden frame, and positional time-series was digitized.

Black winged kite

An individual black-winged kite (*Elanus caeruleus*), residing in the Hula Valley, Israel, was tracked using ATLAS, an innovative reverse-GPS system. ATLAS localizes extremely light-weight, low-cost tags (4), where each tag transmits a distinct radio signal which is detected by a network of base-stations distributed in the study area. Tag localization is computed using nanosecond-scale differences in signal time-of-arrival to each station, alleviating the need to retrieve tags or have power-consuming remote-download capabilities (4, 12). The kite was tracked for 164 consecutive days in years 2019-2020, with a mostly constant tracking frequency of 0.25 Hz.

Similarly to Ref. (12), the kite's tracks are segmented into two behavioral modes, local searches (area restricted search) and commuting (directed flights between local searches). Localizations were segmented by detecting switching points in the data – distinct points in which the bird switches between the two behaviors (44). Switching points were detected using spatiotemporal criteria segmentation, such that localizations that are in proximity to one another, both in space and time were segmented together. In accordance with conclusions of Ref. (12) we independently analyze the time series ensemble that represents instances of local searches and the time series ensemble that represents commuting flights.

White stork

An adult white stork (*Ciconia ciconia*) was tracked between May 2012 and July 2020 using a similar configuration to that of the vulture, see Ref. (36) for more details. Here the GPS location and speed were recorded at a frequency of 1/300 Hz when solar recharge was high (92% of the time), and otherwise every 20 min. We omit days with lower frequency ($< 1\%$ of tracked days) and only include localizations that occur after the first recorded velocity of > 4 m/s (see below).

Eurasian griffon vulture

An Eurasian griffon vulture (*Gyps fulvus*, Hablizl 1783) was tracked in Israel and surrounding countries with high-resolution global positioning system (GPS), between October 2012 and October 2015. The 90-g GPS transmitters (E-Obs GmbH; Munich, Germany) were fitted in a backpack configuration and set to a 13 h duty cycle, between 7:00 a.m. and 8:00 p.m. to correspond with the vulture's activity pattern (37). Localizations were optimally recorded at a frequency of 1/600 Hz (73% of the time for this vulture), or 1/1200 Hz (23 % of the time). Vulture days tracked at lower frequencies were omitted from this study. See Ref. (37) for more details.

As the time of the vulture's departure from the nest can drastically vary between different days, for each tracking day we omit localizations that occur prior to the vulture's first detected movement (37). This was done by removing all localizations that occur before the first recorded velocity of > 4 m/s during the same day.

Continuous-time random walk simulations

In Table 1, in addition to the experimental results, we added results of simulations, which were performed for multiple dynamical models. These models are not intended to fully explain the dynamics

of the experimental systems; rather they can provide valuable insights into the relations between the various exponents. Simulations for several prototypical examples are cited from Ref. (25), whereas CTRW simulations, with an asymptotic power-law waiting-time distribution (see below), for free, bounded and biased random walkers were performed as part of the current study.

CTRW is a random walk defined in terms of the waiting time τ between successive jumps – a random variable drawn from the PDF $\psi(\tau)$. When the average waiting time $\langle\tau\rangle$ diverges, the process displays subdiffusive dynamics, weak ergodicity breaking and aging (7). In accordance with empirical data, see *e.g.* Ref. (12, 51, 52), we assume power-law distributed waiting times, $\psi(\tau) \sim \tau^{-(1+\alpha)}$, for $0 < \alpha < 1$. We simulated three cases: free CTRW, bounded CTRW (BoCTRW), and biased CTRW (BiCTRW) for different values of α . In BoCTRW the random walker is bounded by a confining potential (7), in the sense that it cannot exit predefined domain walls but can move freely within these walls. In BiCTRW the direction of each jump is sampled from a wrapped Cauchy distribution defined by $f(x) = (1 - \rho^2)/[2\pi(1 + \rho^2 - 2\rho \cos x)]$ with $\rho < 1$. In Table 1 we simulated the case of $\rho = 0.3$. The results for BiCTRW match the theoretical results in (28). For all processes we simulated an ensemble of 1000 trajectories of length $t = 1500$ time steps. Notably, for both free and bounded CTRW we obtain similar values of L and M , but for the latter J decreases dramatically due to boundary interactions (7), indicating a transition from positive long-ranged correlations, to anti-correlated motion. Also note that CTRW couples between M and L . For $\alpha < 1$, a negative Moses effect arises due to increasingly long waiting times experienced by the particle as time evolves, which slow down the dynamics. The Noah effect emerges since at most times, the random-walker is stuck in a single location, and practically any jump is a rare event. As α approaches 1, the waiting times become shorter, and jumps become more frequent (on average); hence these effects vanish, and M and L approach $1/2$ (for $\alpha > 1$, $\langle\tau\rangle$ becomes finite, and there is no longer significant aging (11, 28)).

Statistical methods

Local scaling. In several data sets, the scaling regimes fitted to a power-law are local and do not span orders of magnitude. Nonetheless, in all cases reported here, a local scaling exponent can be fitted to the data, in discernible regimes. As the scaling for all four of our empirical quantities is tied through the summation relation, we view the local exponents as a biologically/physically meaningful scaling. Naturally, in few cases, fitting the data in other temporal regimes may reveal slightly different scaling exponent. Yet, we expect all such power-law scaling to maintain the summation relation and to hold significant information at the fitted scale.

Error analysis. For all data sets the fits were performed using SciPy library’s curve-fit (nonlinear least squares method) in python 3.8. In order to satisfy the physical constraint of $L \geq 0.50$ we added bounds to the fits on the mean absolute velocity and mean-squared velocity such that this physical constraint is satisfied (Supplemental Sec. S1.3). As an initial error estimate we took one standard deviation for the parameter of the fitted power-law exponent (error 1). As the local regimes were visually identified, another source of error can be the number of points included in a fitted regime (error 2). To quantify this error we repeated the fit after excluding 5% of data points on the sides of the corresponding regime, and computed the difference between the fits when including these points and when excluding them. In cases where removing the points on the regime boundaries led to large error ($> 10\%$ of a measured exponent) we deduced that no local exponent exist. For instance, when measuring J , denoting by ΔJ_1 and ΔJ_2 error 1 and 2 in J , the total error was $\Delta J = \sqrt{\Delta J_1^2 + \Delta J_2^2}$. Note, that this is taken as the upper bound on the error, since these two sources of error can be correlated. The total error on the predicted value H_p is thus given by

$$\Delta H_p = \sqrt{\Delta J^2 + \Delta M^2 + \Delta L^2}. \quad (5)$$

This formula gives an upper bound of the error on H , as it assumes that the errors on the exponents are independent, which is not necessarily the case for these data.

Missing data points. In several data sets it is common to encounter missing data points in a time series (20). Discarding such time series from the ensemble is possible, but is undesirable. Hence, for any time-series that has $>90\%$ of the points present, we fill missing data points with NaNs, *i.e.*, empty placeholders which are naturally not included in the averaging. To verify that this choice does not affect the statistics, we checked that our results do not change when varying the 90% threshold between 70% and 95%. Furthermore, we checked that in CTRW simulations, randomly replacing 10% of data points with NaNs does not significantly affect the results.

Multidimensional data. Previous works on the Joseph, Moses and Noah effect treated only unidimensional simulations (25–27). Here, we expand the framework to multidimensional data, by reducing two dimensional $[x(t), y(t)]$ to one dimensional time series $|x(t)|$ (Fig. 1). In general, it is not trivial that such a projection will yield results that are similar to any of the original $x(t)$ or $y(t)$. Thus, in the cases studied here we verified that averaging over any of the original variables gives similar results to averaging over their projection.

Acknowledgment

For fieldwork and technical assistance we thank Y. Serry (harvester ants), Y. Orchan and R. Shaish (kite), O. Spiegel and R. Harel (vulture) and S. Rotics and M. Kaatz (stork). EA thanks Andrey Cherstvy and Kevin Bassler for useful discussions and advice. CB acknowledges financial support from Deutsche Forschungsgemeinschaft (DFG), grant SFB1294/1-318763901. AS and MW acknowledge support by the German Academic Exchange Service (PPP USA grant No. 57315749) and by the VolkswagenStiftung (Az. 92738). RN acknowledges support from JNF/KKL grant 60-01-221-18,

BSF grant 255/2008, and DIP (DFG) grant NA 846/1. RN also acknowledges support from Adelina and Massimo Della Pergola Chair of Life Sciences. RM acknowledges the German Science Foundation (DFG) for support within grant ME 1535/12-1. OV and MA acknowledge support from the ISF grant 531/20. MA also acknowledges Alexander von Humboldt Foundation for an experienced researcher fellowship.

Author Contributions

OV, EA, RM and MA conceived and planned the study. OV, EA and MA performed the analytical calculations and analyzed the data. OV wrote the numerical code and performed the simulations. TA, CB, ON, AS, RS, DS, MW, DK and RN performed the experiments and collected the data. OV, EA and MA wrote the manuscript with valuable input from all other authors.

Competing Interests statement

The authors declare no competing interests.

Appendix

1 Statistical methods

1.1 Derivation and violations of the Gaussian CLT

We present here a well-known pedestrian derivation of the Gaussian CLT (53) with emphasis on the assumptions of the theorem, which can be violated when the increments are non-stationary or long-ranged (or anti-) correlated, or if their mean-square is not finite.

Consider, without loss of generality, the series of identically distributed random numbers $\delta x_0, \delta x_1, \dots, \delta x_{n-1}$, with zero mean and variance $\sigma^2 > 0$ (which also equals the second moment in this case), as increments of the one-dimensional discrete process $x_n = x_0 + \sum_{i=0}^{n-1} \delta x_i$. We define the probability density $W(\delta x_i) \equiv W(x_{i+1} - x_i)$, of traveling the distance $x_{i+1} - x_i$, for $i = 0..n - 1$. If the increments are *identically distributed*, and do not depend explicitly on location and time, the probability distribution $P(x, n)$ of being at $x_n = x$ after n steps, is given by the recurrence equation $P(x, n) = \int_{-\infty}^{\infty} dx_{n-1} W(x_n - x_{n-1}) P(x_{n-1}, n - 1)$. Initially we assume that $x_0 = 0$, namely $P(x, 0) = \delta(x_0)$, where $\delta(\cdot)$ is the Dirac delta function. Since $x_0 = x_n - \sum_{i=0}^{n-1} \delta x_i$, and $\delta(x)$ is symmetric, one can write

$$P(x, n) = \int_{-\infty}^{\infty} d\delta x_{n-1} \int_{-\infty}^{\infty} d\delta x_{n-2} \dots \int_{-\infty}^{\infty} d\delta x_0 W(\delta x_{n-1}) W(\delta x_{n-2}) \dots W(\delta x_0) \delta \left(x - \sum_{i=1}^n \delta x_i \right). \quad (\text{A1})$$

Defining the Fourier transform as $f(x) \rightarrow \hat{f}(k) = \int_{-\infty}^{\infty} f(x) e^{ikx} dx$, and using the relation

$\int_{-\infty}^{\infty} dx \delta \left(x - \sum_{i=1}^n \delta x_i \right) e^{ikx} = e^{ik \sum_{i=0}^{n-1} \delta x_i}$, if the increments are also *independent*, we can separate

the integrals in Eq. (A1) and write

$$\hat{P}(k, n) = \left(\int_{-\infty}^{\infty} dx_{n-1} W(\delta x_{n-1}) e^{ik\delta x_{n-1}} \right) \left(\int_{-\infty}^{\infty} dx_{n-2} W(\delta x_{n-2}) e^{ik\delta x_{n-2}} \right) \dots \left(\int_{-\infty}^{\infty} dx_0 W(\delta x_0) e^{ik\delta x_0} \right) = [\hat{W}(k)]^n. \quad (\text{A2})$$

Finally, if the increment variance is finite, it can be shown that in the limit $k \rightarrow 0$ (associated with large δx_i), one has $\hat{W}(k) \simeq 1 - \sigma^2 k^2 / 2$ (53). Using this, and performing the inverse Fourier transform $\hat{f}(x) \rightarrow f(k) = \frac{1}{2\pi} \int_{-\infty}^{\infty} f(x) e^{-ikx} dx$, we obtain $P(x, n) = \frac{1}{\sqrt{2\pi\sigma^2 n}} \exp[-x^2 / (2n\sigma^2)]$, a Gaussian distribution, as expected.

Violations of this derivation occur in the following scenarios: (i) If the increment PDF explicitly depends on time (Moses effect), in Eq. (A1); $W(\delta x_i) \rightarrow W(\delta x_i, i)$. Thus, the relation $\hat{P}(k, n) = [\hat{W}(k)]^n$ is no longer valid, since $\hat{W}(k) \rightarrow \hat{W}(k, i)$ depends on i , and this may lead to time dependence in the product $\hat{W}(k, 0)\hat{W}(k, 1)\dots\hat{W}(k, n-1)$. (ii) In the presence of temporal autocorrelations (Joseph effect), the integrals cannot be separated, rendering Eq. (A2) invalid. (iii) If the variance of the increments is infinite (Noah effect), the asymptotic shape of $\hat{W}(k)$ may include non-integer power-laws in k yielding a nonlinear in time MSD.

1.2 Evaluation of the Joseph exponent J from the TAMSD

The Joseph exponent J is defined via the scaling of the integrated velocity-autocorrelation function, with respect to the time-gap between the two points (26)

$$\int_0^s \frac{\langle \mathbf{v}(t) \cdot \mathbf{v}(t+s') \rangle}{\langle \mathbf{v}^2(t) \rangle} ds' \propto s^{2J-1}, \quad (\text{A3})$$

for $s \in [s_c, \infty)$, and $s_c > 0$ is some lower cutoff. The autocorrelation function $\langle \mathbf{v}(t) \cdot \mathbf{v}(t+s') \rangle$, however, is often difficult to measure directly from data, since it requires a very large ensemble of

long trajectories to overcome the noise. For this reason, several alternative numerical methods have been developed to measure this exponent from various other observables, that are mathematically linked to Eq. (A3), see e.g. Refs. (23, 25, 54, 55).

We chose to compute J using Eq. (3) in the main text [Eq. (A8) below], which is computationally inexpensive in comparison with the other techniques, and easy to implement. Here we generalize the derivation of the link between Eqs. (A3) and (3) (26, 56) for $d \geq 1$ dimensions. We start from the TAMSD

$$\langle \overline{\delta^2(s, t)} \rangle \approx \frac{1}{t-s} \int_0^{t-s} \langle [\mathbf{x}(t'+s) - \mathbf{x}(t')]^2 \rangle dt'. \quad (\text{A4})$$

Focusing on the long time limit and also assuming $t \gg s$, we can use the Green-Kubo relation to write (56)

$$\langle [\mathbf{x}(t'+s) - \mathbf{x}(t')]^2 \rangle = 2 \int_0^s dt_2 \int_0^{t_2} dt_1 \langle \mathbf{v}(t_1+t') \cdot \mathbf{v}(t_2+t') \rangle. \quad (\text{A5})$$

Equations (A4, A5) tie between the asymptotic scaling shape of the TAMSD and the autocorrelation function, given by Eq. (A3). The crux of the derivations in (26, 56) is to write the autocorrelation function in a general scaling form, depending on the properties of the process, which eventually lead to $\langle \overline{\delta(s, t)} \rangle \sim t^{2M+2L-1} s^{2J}$. This scaling, although different from that of the autocorrelation function, allows finding the exponent J in an independent manner from M and L , see main text. Note that, these derivations were originally done in one dimension, but can be easily extended to the scalar product $\langle \mathbf{v}(t_1+t') \cdot \mathbf{v}(t_2+t') \rangle$. In addition, the details of the derivation depend on the properties of the autocorrelation function, e.g., whether J is above or below $1/2$.

Although the TAMSD is a very convenient observable, both from the interpretation point of view and measurement perspective, when comparing between the sum of the exponents $J + M + L - 1$

and H (see Fig. 5 in the main text), our numerical results do not fully restore the summation relation in Eq. (4) in the main text. Instead, a small difference of $\sim 4\%$ on average is observed. To study this discrepancy, we have compared between the predictions for J of different methods, obtained from ensembles of simulated fractional Brownian motion paths with various values of J . Based on our results (not shown), we find that extracting J from the TAMSD gives rise to a slight underestimation of the true value of the Joseph exponent, when the ensemble size is small and/or the trajectories are short. In this case, one may use other methods to estimate J , such as wavelets (54). However, as the length of the trajectories or ensemble size are increased, we checked that the values of J converge to the true known value of the simulation.

1.3 Measuring the exponents

Below, is the recipe we use to generate a time-series from raw empirical data, and obtain the exponents M , L and J for an ensemble of paths.

1. We choose a constant sampling frequency, to generate uniformly sampled time-series from the raw data sets. If a small percentage of the time series is missing in the data ($< 10\%$), the missing locations are treated as NaNs and are excluded from any averaging (see methods in the main text).
2. For each trajectory $\mathbf{x}(t)$ in $d \geq 1$ dimensions, in the time interval $t \in [0, T]$, we choose an additional constant time increment of duration $0 < \Delta \ll t$. The size of Δ should be larger than the sampling rate of the data, but much smaller than the total duration of the time series. For different values of $\Delta \ll t$, we obtain

(a) Time-averaged absolute velocity

$$\overline{|\mathbf{v}|}(t) \equiv \frac{1}{t - \Delta} \sum_{j=1}^{t/\Delta} \frac{|\delta \mathbf{x}_j|}{\Delta} \quad (\text{A6})$$

where $\delta \mathbf{x}_j \equiv \mathbf{x}(j\Delta) - \mathbf{x}([j - 1]\Delta)$ is the j th vector-increment of the path.

(b) Time-averaged squared velocity

$$\overline{\mathbf{v}^2}(t) \equiv \frac{1}{t - \Delta} \sum_{j=1}^{t/\Delta} \frac{(|\delta \mathbf{x}_j|)^2}{\Delta^2}. \quad (\text{A7})$$

3. For each trajectory, compute the time averaged squared displacement

$$\overline{\delta^2(s, t)} \equiv \frac{1}{t - s} \int_0^{t-s} [\mathbf{x}(t' + s) - \mathbf{x}(t')]^2 dt', \quad (\text{A8})$$

as a function of s .

4. After repeating steps 2 and 3 for all the time series, we can compute the ensemble average of the quantities above, for each time t [in the case of Eqs. (A6) and (A7)], and each value of $s \in [1, \lfloor t/4 \rfloor]$ [in the case of Eq. (A8)] over all time-series in the ensemble.

5. By plotting the statistics (see main text and Sec. 2) we visually identify regimes that can be described by local scaling exponents. We then fit each regime with a power law using the method of non-linear least squares. The fit is performed using *SciPy* library in python 3.8. In order to satisfy the physical constraint of $L \geq 0.50$ we add this bound by first fitting $\langle \overline{\mathbf{v}^2} \rangle$ to a scaling exponent, and then constraining the fit of $\langle \overline{|\mathbf{v}|} \rangle$ in order to satisfy Eq. (2) of the main text under the condition that $L > 0.50$. Note that, when applying power-law fits to data, one may consider to apply additional statistical tests to gain confidence about the results of the local exponents.

2 Data analysis for all datasets

Here we present the statistics for data sets that are not plotted in the main text. All exponents that result from these statistics are detailed in Table 1 of the main text.

2.1 Fluorescent Rhodamine molecules

Here we plot the statistics for the fluorescent Rhodamine molecules in different relative humidity (see main text). Here, for all humidities, the trajectories are two dimensional and are acquired at an acquisition time of $\Delta = 50$ ms, for at least 1500 ms (some trajectories are longer). For the values of the exponents, see Table 1 in the main text.

In Fig. A1, A2, A3, A4 and A5 we plot the statistics for relative humidity of 100%, 90%, 85%, 75% and 30%, where the statistics are averaged over an ensemble of 174, 298, 239, 258 and 436 trajectories, respectively.

2.2 Tracers in cells

In Fig. A6 we plot the statistics for the tracers (quantum dots) in cytoplasm of treated mammalian cells (see main text). In Fig. A7 we plot the statistics for the untreated cells. The results of the analysis (see Table 1 in main text) are consistent with the analyses performed in (21). There, it has been shown that the mean scaling exponent of TA-MSDs (and their geometric ensemble average) for short time scales ($t < 1s$) is very similar in both untreated and treated cells ($\alpha \approx 0.58$, cf. [21]). The average diffusion coefficient, however, was seen to be significantly lower for the ensemble of longer trajectories, highlighting a bias of long trajectories for lower mobilities. Strong fluctuations in the diffusion coefficient of individual trajectories also led to an overestimation of the short-term scaling exponent in both cases when using an arithmetic instead of a geometric averaging ($\alpha \approx 0.78$, cf.

[21]). In fact, an arithmetic average is equivalent to the definition of Eq. 4 of the main text, predicting a value $J = \alpha/2 \approx 0.39$ for short time scales in both ensembles, in excellent agreement with our findings here. Fitting the arithmetic ensemble average of all TA-MSDs on time scales $\tau > 2$ s yielded an average scaling exponent $\alpha = 1.12 \pm 0.07$ for untreated and $\alpha = 0.90 \pm 0.02$ for latrunculin-treated cells, in good agreement with $J = 0.61$ and $J = 0.50$ in Table 1 of the main text.

2.3 Harvester ants

In Fig. A8 we plot the statistics for the harvester ants.

2.4 Black winged kites

For the kites we analyze independently the ensemble of commuting trajectories and area restricted searches, see main text. In Fig. A9 and A10 we respectively plot the statistics for the commuting and searching kite, averaged over an ensemble of 1516 and 2557 two-dimensional trajectories (recorded as locations in the Hula Valley local map), each measured at a frequency of 0.25 Hz.

3 Aging and the Moses effect

In data sets with a measurable Moses effect, it is plausible that the data set also shows statistical aging (see main text). Thus, the time of start of measurement can play a crucial role in determining the statistics of an experimental system [7, 52].

To show this we use the ensemble of kite search flights described above, and we age the system by "starting" each trajectory 10 min after first recorded measurement of that search. In Fig. A11 we plot the statistics for this aged ensemble. The parameters now vary between two temporal regimes, and assume different values than those we find for the unaged system. Here, for the aged system, at

times $0.1 < t < 5$ min we find $J = 0.26$, $M = 0.46$, $L = 0.50$ and $H = 0.23$ (the summation relation predicts $H = 0.22$) and at times $5 < t < 20$ min we find $J = 0.23$, $M = 0.38$, $L = 0.52$ and $H = 0.14$ (the summation relation predicts $H = 0.12$). As expected, the long range correlations are not strongly affected by the aging (7). However, the Moses and Noah effects are significantly obscured by aging, although the summation relation still gives a valid prediction. These results entail that in order to fully capture a systems statistics, initiating the measurement at the beginning of the process can prove crucial. Ecologically, to describe any non-ergodic behavioral mode, one has to have the ability to measure the process from its beginning (this is both a conceptual challenge and a technical one, but it underlies our ability to get meaningful results from ecological tracking).

4 Continuous-time random walk simulations

In the main text we present results from CTRW simulations. Here we provide an example for statistics obtained from one simulation. In Fig. A12 we plot the statistics for free CTRW for $\alpha = 0.4$. Here we average 1000 simulations of 5000 points. The values for the exponents are provided in Table 1 of the main text.

References

1. S. R. P. Pavani, *et al.*, *Proc. Natl. Acad. Sci. USA* **106**, 2995 (2009).
2. H. Shen, *et al.*, *Chem. Rev.* **117**, 7331 (2017).
3. N. E. Humphries, H. Weimerskirch, N. Queiroz, E. J. Southall, D. W. Sims, *Proc. Natl. Acad. Sci. USA* **109**, 7169 (2012).
4. S. Toledo, *et al.*, *Science* **369**, 188 (2020).

5. V. Méndez, D. Campos, F. Bartumeus, *Stochastic foundations in movement ecology* (Springer, 2016).
6. V. Zaburdaev, S. Denisov, J. Klafter, *Rev. Mod. Phys.* **87**, 483 (2015).
7. R. Metzler, J.-H. Jeon, A. G. Cherstvy, E. Barkai, *Phys. Chem. Chem. Phys.* **16**, 24128 (2014).
8. M. Kozłowska, R. Kutner, *Physica A* **357**, 282 (2005).
9. M. Assaf, B. Meerson, *J. Phys. A Math. Theor.* **50**, 263001 (2017).
10. J.-P. Bouchaud, *J. Phys. I* **2**, 1705 (1992).
11. S. Burov, J.-H. Jeon, R. Metzler, E. Barkai, *Phys. Chem. Chem. Phys.* **13**, 1800 (2011).
12. O. Vilch, *et al.*, *E-print arXiv:2101.11527* .
13. J. Szymanski, M. Weiss, *Phys. Rev. Lett.* **103**, 038102 (2009).
14. P. Massignan, *et al.*, *Phys. Rev. Lett.* **112**, 150603 (2014).
15. D. Krapf, *Current topics in membranes* **75**, 167 (2015).
16. A. G. Cherstvy, S. Thapa, C. E. Wagner, R. Metzler, *Soft Matter* **15**, 2526 (2019).
17. R. Nathan, *et al.*, *Proc. Natl. Acad. Sci. USA* **105**, 19052 (2008).
18. I. Chakraborty, G. Rahamim, R. Avinery, Y. Roichman, R. Beck, *Nano Lett.* **19**, 6524 (2019).
19. J. Janczura, *et al.*, *New J. Phys.* **23**, 053018 (2021).
20. C. H. Fleming, *et al.*, *Am. Nat.* **183**, E154 (2014).

21. A. Sabri, X. Xu, D. Krapf, M. Weiss, *Phys. Rev. Lett.* **125**, 058101 (2020).
22. S. Thapa, *et al.*, *E-print arXiv:2005.02099* (2020).
23. G. Muñoz-Gil, *et al.* (2021).
24. B. B. Mandelbrot, J. R. Wallis, *Water Resour. Res.* **4**, 909 (1968).
25. L. Chen, K. E. Bassler, J. L. McCauley, G. H. Gunaratne, *Phys. Rev. E* **95**, 042141 (2017).
26. E. Aghion, P. G. Meyer, V. Adlakha, H. Kantz, K. E. Bassler, *New J. Phys.* **23**, 023002 (2021).
27. P. G. Meyer, V. Adlakha, H. Kantz, K. E. Bassler, *New J. Phys.* **20**, 113033 (2018).
28. G. Bel, E. Barkai, *Phys. Rev. Lett.* **94**, 240602 (2005).
29. G. M. Viswanathan, M. G. Da Luz, E. P. Raposo, H. E. Stanley, *The physics of foraging: an introduction to random searches and biological encounters* (Cambridge University Press, Cambridge UK, 2011).
30. V. Paxson, S. Floyd, *IEEE ACM Trans. Netw.* **3**, 226 (1995).
31. I. I. Eliazar, M. F. Shlesinger, *Phys. Rep.* **527**, 101 (2013).
32. M. Zamani, E. Aghion, P. Pollner, T. Vicsek, H. Kantz, *arXiv preprint arXiv:2106.10038* (2021).
33. R. Sarfati, D. K. Schwartz, *ACS Nano* **14**, 3041 (2020).
34. A. G. Cherstvy, O. Nagel, C. Beta, R. Metzler, *Phys. Chem. Chem. Phys.* **20**, 23034 (2018).
35. T. Avgar, I. Giladi, R. Nathan, *Ecol. Lett.* **11**, 224 (2008).

36. S. Rotics, *et al.*, *J. Anim. Ecol.* **85**, 938 (2016).
37. R. Harel, *et al.*, *Philos. Trans. R. Soc. Lond., B, Biol. Sci.* **371**, 20150397 (2016).
38. M. J. Skaug, J. Mabry, D. K. Schwartz, *Phys. Rev. Lett.* **110**, 256101 (2013).
39. D. Wang, D. K. Schwartz, *J. Phys. Chem. C* **124**, 19880 (2020).
40. M. Guo, *et al.*, *Cell* **158**, 822 (2011).
41. L. Stadler, M. Weiss, *New J. Phys.* **19**, 113048 (2017).
42. K. Speckner, L. Stadler, M. Weiss, *Phys. Rev. E* **98**, 012406 (2018).
43. S. Benhamou, *Ecology* **88**, 1962 (2007).
44. S. Benhamou, *Ecol. Lett.* **17**, 261 (2014).
45. O. Spiegel, *et al.*, *Am. Nat.* **185**, E44 (2015).
46. I. van Coppenolle, P. Aerts, *Anim. Biol.* **54**, 281 (2004).
47. N. Horvitz, *et al.*, *Ecol. Lett.* **17**, 670 (2014).
48. M. Mangalam, D. G. Kelty-Stephen, *Neurosci. Biobehav. Rev.* (2021).
49. Y. Meroz, I. M. Sokolov, *Phys. Rep.* **573**, 1 (2015).
50. M. Auger-Méthé, A. E. Derocher, M. J. Plank, E. A. Codling, M. A. Lewis, *Methods Ecol. Evol.* **6**, 1179 (2015).
51. X. Brokmann, *et al.*, *Phys. Rev. Lett.* **90**, 120601 (2003).

52. M. S. Song, H. C. Moon, J.-H. Jeon, H. Y. Park, *Nat. Comm.* **9**, 1 (2018).
53. J. Klafter, I. M. Sokolov, “*First steps in random walks: from tools to applications*” (Oxford University Press, Oxford UK, 2011).
54. P. Abry, D. Veitch, *IEEE Trans. Inf. Theory* **44**, 2 (1998).
55. M. Höll, K. Kiyono, H. Kantz, *Phys. Rev. E* **99**, 033305 (2019).
56. P. Meyer, E. Barkai, H. Kantz, *Phys. Rev. E* **96**, 062122 (2017).

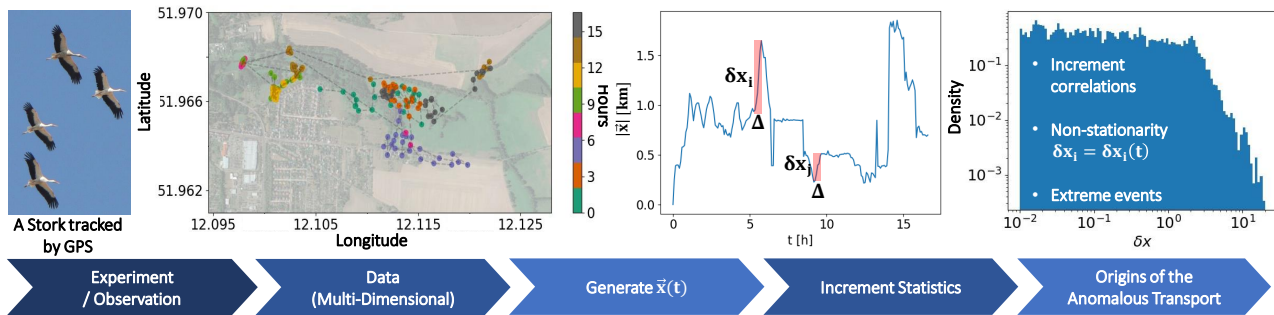


Figure 1: Scheme of the three-effect decomposition of the origins of anomalous transport measured in data. (left to right) 1. Collect data from an experiment. 2. The observation or experiment generates multidimensional paths, *e.g.*, a flight pattern of a stork tracked by GPS over several hours. 3. Generate the time series $\vec{x}(t) \equiv \mathbf{x}(t)$, and decompose it into vector increments $\delta\mathbf{x}_i = \mathbf{x}_{i\Delta} - \mathbf{x}_{(i-1)\Delta}$ ($i = 1, \dots, N$) of equal duration $0 < \Delta \ll t$. 4. Obtain the statistics of increment sizes. 5. Determine whether the process is correlated, explicitly time-dependent, or susceptible to extreme fluctuations since its velocity PDF contains a fat tail.

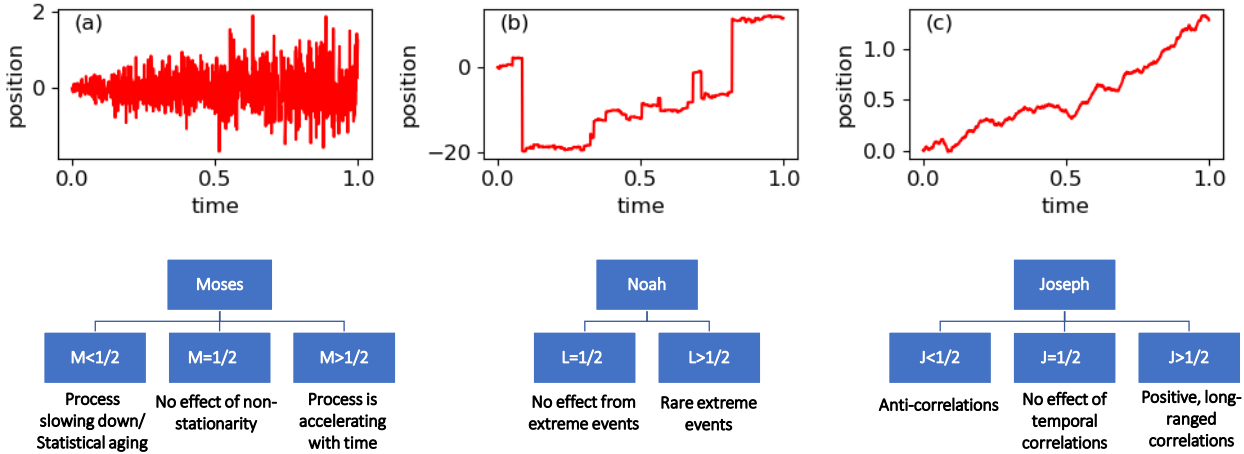


Figure 2: Prototypical examples of processes displaying anomalous diffusion. (a) An non-stationary accelerating process (scaled Brownian motion), leading to the *Moses* effect. This can result, *e.g.*, from movement in a (temporal) temperature gradient increasing fluctuations over time. (b) A process with rare extreme events (Lévy flight), leading to the *Noah* effect. Such a process has been used, *e.g.*, to model flight patterns of the wandering albatross (29), but this characterization is under debate (43). (c) A process with long ranged temporal correlations (fractional Brownian motion), giving rise to a trended motion, and the *Joseph* effect. This may result, *e.g.*, from long-range memory in network traffic (30, 31). In all three panels, due to different violations of the CLT the rate of diffusion is different than in normal diffusion. In addition, position and time are shown in arbitrary units. Lower panels: The physical interpretation of the values of the Moses, Noah and Joseph exponents. (i) A Moses effect is a proxy for non-stationarity. Here $M > 1/2$ and $M < 1/2$ respectively indicate an accelerating and decelerating process (the latter entails aging), whereas for $M = 1/2$ the process is stationary. (ii) A Noah effect is a proxy for detecting extreme rare events. Here $L > 1/2$ indicates susceptibility to large fluctuations due to a fat-tailed velocity PDF, whereas for $L = 1/2$ no Noah effect occurs. (iii) A Joseph effect is a proxy for long-range or anti- correlations. Here $J > 1/2$ indicates long-range positive temporal correlations which may lead to superdiffusion, and $J < 1/2$ indicates anti- correlations which may lead to subdiffusion. When $J = 1/2$ no Joseph effect occurs.

dataset	ensemble size	regime	J	L	M	H measured	H prediction	$\frac{ H_p - H }{H}$
Rhodamine	174	50 < t < 1500 ms	0.50	0.50	0.41	0.38 ± 0.02	0.42 ± 0.04	10%
Rhodamine 100%								
Rhodamine 90%	298	50 < t < 1500 ms	0.38	0.50	0.42	0.28 ± 0.02	0.30 ± 0.03	7%
Rhodamine 85%	239	50 < t < 1500 ms	0.34	0.50	0.40	0.22 ± 0.02	0.24 ± 0.05	9%
Rhodamine 75%	258	50 < t < 1500 ms	0.22	0.51	0.44	0.18 ± 0.02	0.18 ± 0.01	>1%
Rhodamine 30%	436	50 < t < 1500 ms	0.09	0.50	0.44	0.07 ± 0.02	0.04 ± 0.03	**
Tracers in treated cells	200	0.1 < t < 5 s	0.39	0.50	0.41	0.31 ± 0.01	0.30 ± 0.02	3%
		5 < t < 50 s	0.50	0.50	0.44	0.44 ± 0.01	0.44 ± 0.01	<1%
Tracers in untreated cells	1000	0.1 < t < 2 s	0.39	0.50	0.44	0.31 ± 0.01	0.33 ± 0.02	6%
		2 < t < 8 s	0.60	0.50	0.47	0.55 ± 0.01	0.57 ± 0.01	4%
Amoeba	1142	1 < t < 6 min	0.61	0.50	0.44	0.58 ± 0.01	0.55 ± 0.03	5%
		10 < t < 100 min	0.52	0.52	0.37	0.42 ± 0.02	0.40 ± 0.02	5%
Harvester ants	67	10 < t < 100 s	0.88	0.50	0.57	0.92 ± 0.12	0.95 ± 0.08	3%
		100 < t < 400 s	0.59	0.51	0.35	0.47 ± 0.03	0.45 ± 0.03	4%
Commuting kite	107	0.1 < t < 3 min	0.87	0.50	0.49	0.84 ± 0.02	0.86 ± 0.02	2%
		3 < t < 12 min	0.80	0.50	0.50	0.76 ± 0.01	0.80 ± 0.02	5%
Searching kite	587	0.5 < t < 20 min	0.24	0.59	0.22	0.06 ± 0.02	0.06 ± 0.01	<1%
Stork (Jun-Jul)	455	0.2 < t < 2 h	0.46	0.88	-0.24	*	0.10 ± 0.03	-
		2 < t < 10 h	0.18	0.50	0.48	*	0.16 ± 0.08	-
Stork (Aug-Sep)	394	0.2 < t < 2 h	0.98	0.55	0.55	1.20 ± 0.03	1.08 ± 0.02	10%
		2 < t < 10 h	0.84	0.50	0.70	1.03 ± 0.01	1.04 ± 0.06	1%
Stork (Oct-Jan)	854	0.2 < t < 2 h	0.78	0.66	0.25	0.74 ± 0.02	0.68 ± 0.03	8%
		2 < t < 10 h	0.57	0.50	0.65	0.80 ± 0.02	0.73 ± 0.10	9%
Stork (Mar-Apr)	391	0.2 < t < 2 h	0.98	0.51	0.55	1.08 ± 0.02	1.04 ± 0.02	4%
		2 < t < 10 h	0.80	0.50	0.65	1.01 ± 0.01	0.95 ± 0.07	6%
Vulture	444	0.1 < t < 2 h	0.75	0.50	0.58	0.82 ± 0.02	0.84 ± 0.02	1%
		2 < t < 5.5 h	0.57	0.50	0.63	0.76 ± 0.02	0.70 ± 0.04	9%
Simulations	ensemble size	parameters						
Brownian motion			0.50	0.50	0.50	0.50	0.50	<1%
SBM	10 ⁵	M = 0.3	0.50	0.50	0.30	0.30	0.30	<1%
LF	10 ⁵	L = 0.71	0.50	0.71	0.50	0.71	0.71	<1%
FBM	10 ⁵	J = 0.3	0.30	0.50	0.50	0.30	0.30	<1%
FBM	10 ⁵	J = 0.7	0.70	0.50	0.50	0.70	0.70	<1%
SFBM	10 ⁵	J=M=0.7	0.70	0.50	0.70	0.90	0.90	<1%
SFLM	10 ⁵	J=L=0.6, M=0.3	0.60	0.60	0.30	0.50	0.50	<1%
CTRW	10 ³	$\alpha = 0.8$	0.50	0.62	0.27	0.38 ± 0.01	0.38 ± 0.01	<1%
CTRW	10 ³	$\alpha = 0.4$	0.50	0.80	-0.11	0.21 ± 0.01	0.20 ± 0.01	5%
BoCTRW	10 ³	$\alpha = 0.7$	0.15	0.66	0.18	0 ± 0.01	-0.01 ± 0.01	*
BiCTRW	10 ³	$\alpha = 0.8$	0.92	0.63	0.24	0.75	0.78	4%
BiBM	10 ³		1	0.5	0.5	1	1	<1%

Table 1: Summary of the decomposition of the origins of anomalous diffusion, in various data sets and simulations. We present the evaluated error on both H and H_p , see Methods (* mark instances where the MSD could not be fitted to a power-law due to considerable noise). We also present the relative error between the directly-measured value of H and its prediction via the sum rule (4), $|H_p - H|/H$ in percentages. In cases where the relative error of either the observed or predicted values exceeds the difference between the two, we assume good agreement regardless of the relative error, which can naturally be large for small values of the Hurst exponent (** mark instances where the difference between the measurement and predicted H is smaller than the errors on H). The simulations represent some prototypical examples of anomalous processes, and obey the summation relation. CTRW simulations were done in the current study, and all other simulated systems are results quoted from Ref. (25). Legend: BM = Brownian Motion. SBM = Scaled BM. LM = Lévy Motion (a.k.a., Lévy flight). FBM = Fractional BM. SFBM = Scaled FBM. SFLM = Scaled Fractional LM. CTRW = Continuous-Time Random Walk. BoCTRW = Bounded CTRW. BiCTRW = Biased CTRW. BiBM = Biased Brownian motion. Note that the errors in simulations quoted from (25) are less than 10^{-4} .

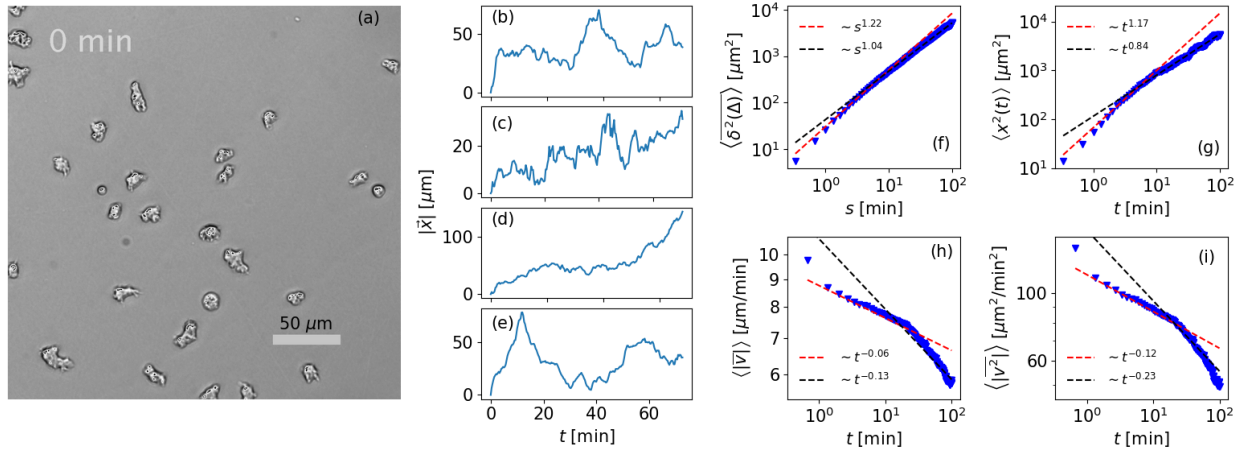


Figure 3: Amoeba: from raw data to statistics – depiction of the workflow repeated for all empirical setups. Panel (a) is a snapshot of tracked amoeba, measured experimentally in (34). From the two-dimensional paths, we generate vector trajectories for $\mathbf{x}(t)$, which we decompose into increments and obtain one-dimensional paths indicating the distance traveled as a function of time [Panels (b-e)]. For each time series, and measurement time t , we compute TAs, followed by EAs, for the squared-displacement $\delta^2(s)$ (f), absolute-velocity $|\mathbf{v}(t)|$ (h), and squared-velocity $\mathbf{v}^2(t)$ (i). To independently measure the exponent H , we further obtain the MSD $\mathbf{x}^2(t)$ (g). Using the increment statistics in panels (f-i) we visually identify two regimes, $1 < t < 6$ min and $10 < t < 100$ min, that fit local scaling exponents (“local” here means within a certain finite period of time, see Methods), and each regime is then fitted to a power-law using the method of nonlinear least-squares. The measured values are marked in blue triangles and the fits are plotted as red and black dashed lines for the first and second regimes, respectively. The fit values are given in the legends, and are used to extract the scaling exponents J, L, M and H . Specifically, J and H are extracted from panels (f) and (g) respectively by dividing the fitted values by 2, M is extracted from panel (h) by adding $1/2$ to the fitted value, and L is extracted from panel (i), using the previously found value of M [see Eq. (2)].

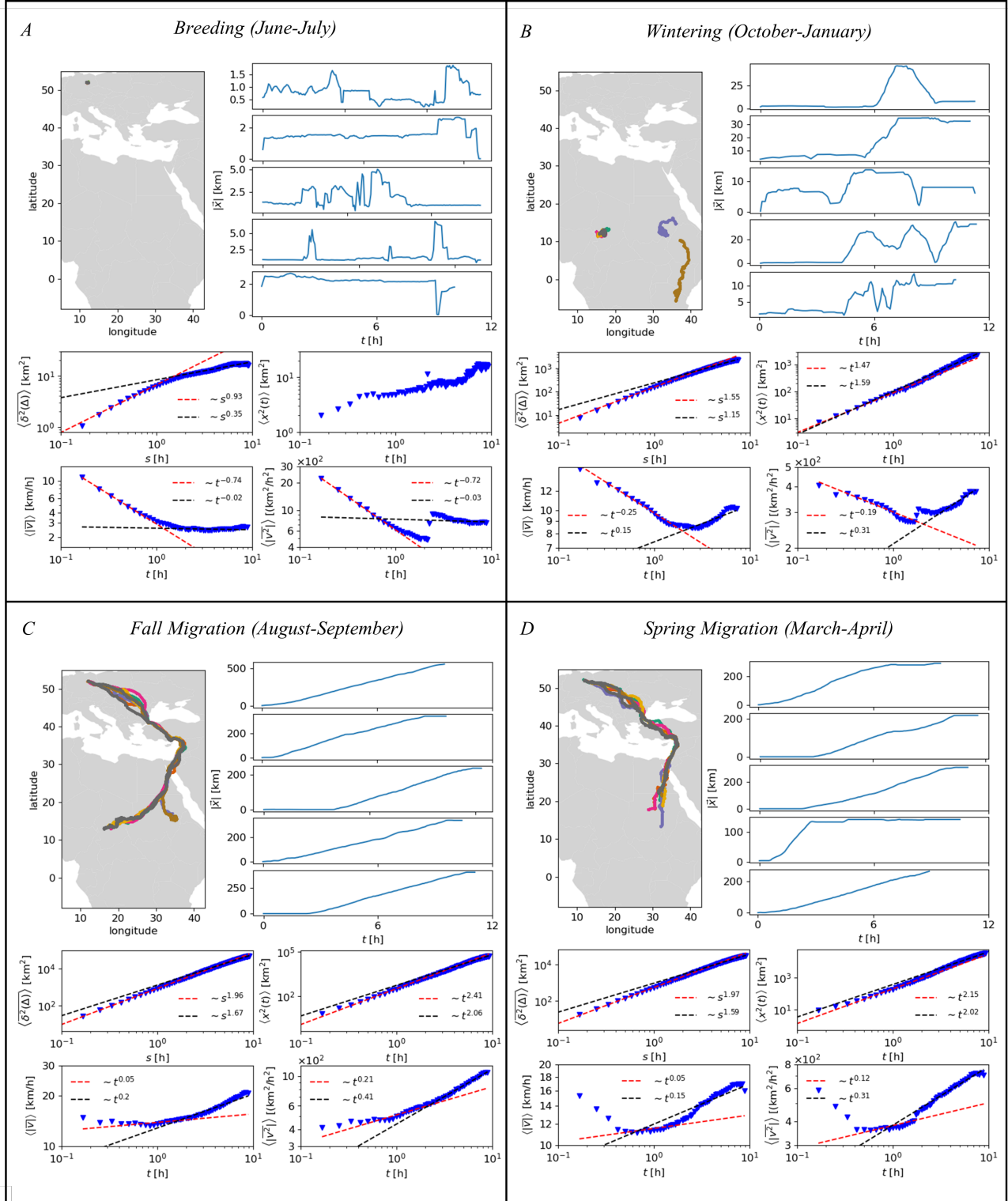


Figure 4: The white stork: from raw data to statistics during four periods: June-July (A), October-January (B), August-September (C) and March-April (D). In each box (A-D), the upper left panels are GPS tracks, where different colors represent different years. The five upper right panels are examples for the distance traveled at a single day as a function of the time of measurement in hours. The four lower panels are the statistics on the ensemble of days during the relevant period, and the fit values are given in the plot legends (see Fig. 3 for details). Notably, in A the MSD could not be fitted to a power-law, due to considerable noise, yet the value of H can still be estimated from the other exponents using Eq. (4).

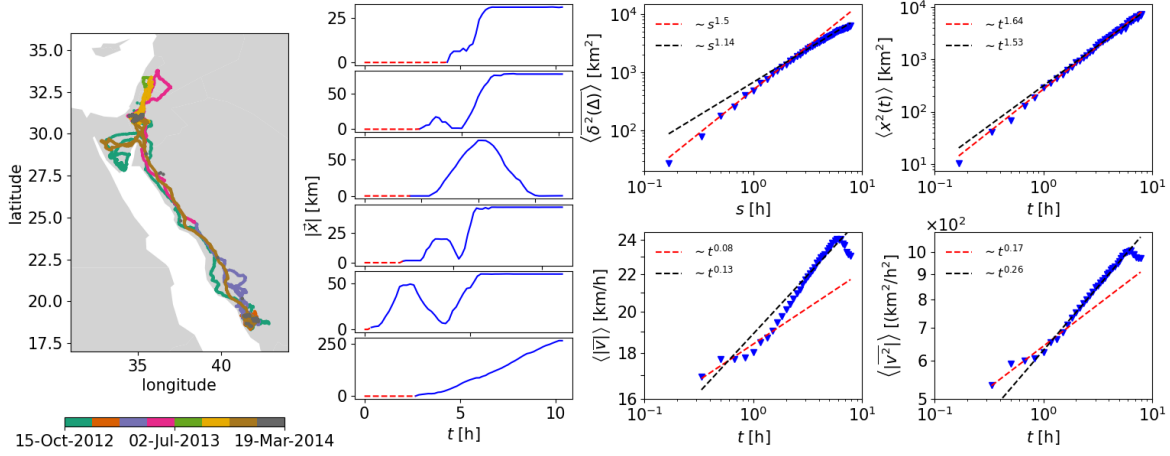


Figure 5: Vulture: from raw data to statistics. Left panel: GPS tracks of the vulture. Middle panels: examples for the distance traveled (km) as a function of time (hours). As was done in Ref. (37), the individual paths are normalized to start at the first relocation in the day for which the GPS records velocity of >4 m/s, as to avoid aging of the system due to long initial waiting times. The red dashed lines represent initial stationary periods of the animal. Four right panels: statistics fitted in two regimes, for $0.1 < t < 2$ h and for $2 < t < 5.5$ h (see Fig. 3 for details).

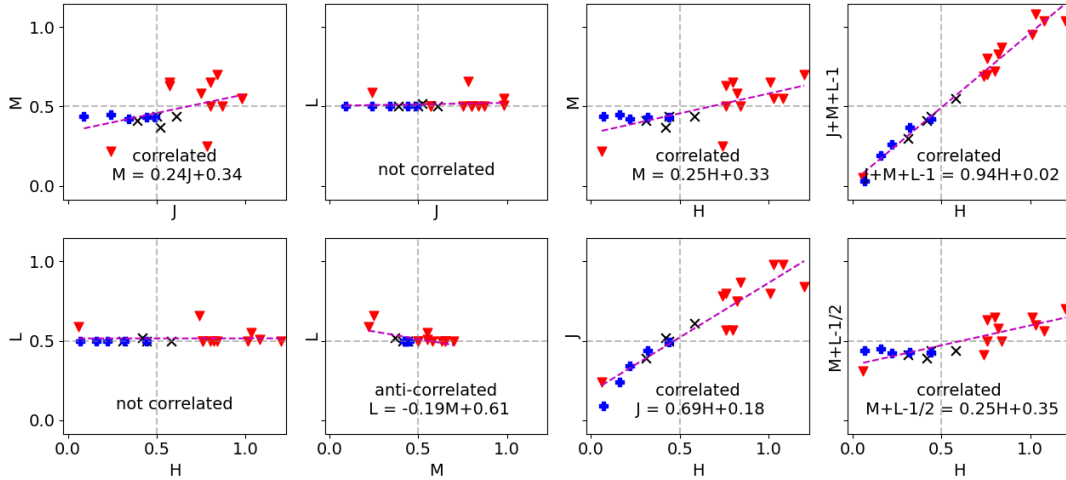


Figure 6: The correlations between any two exponents measured for the empirical systems, as well as the relation between H and the prediction of the summation relation. Blue pluses mark the chemical data sets, black \times mark the biological data sets, and red triangles mark the ecological data sets. The size of each marker reflects a typical (average) error of 0.03. The purple dashed line represents a linear least square fit. The data was assumed to be correlated (anti-correlated) if Pearson's correlation coefficient test showed a p-value < 0.05 and yielded a positive (negative) test statistics. For (anti-)correlated fits the results of the linear fit are explicitly written. Note, that we have omitted two points from the analysis (a stork in the breeding season), since the H value there could not be determined.

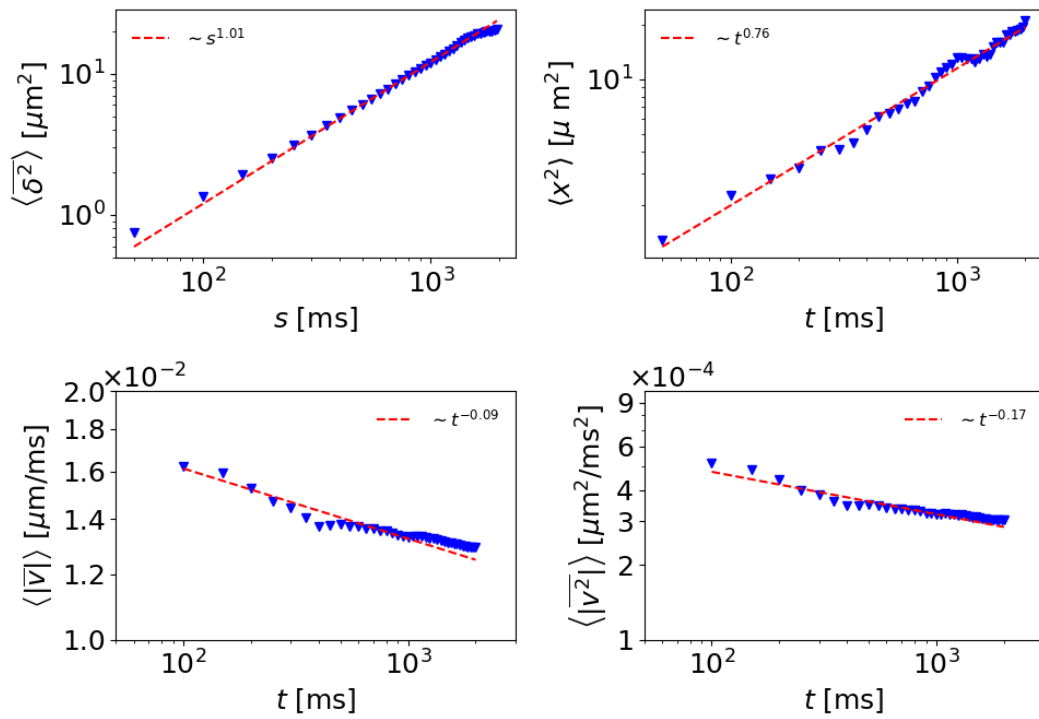


Figure A1: Statistics for fluorescent Rhodamine molecules with relative humidity of 100%. All panels were fitted in the range $50 < t < 1500$ ms. Measured values are plotted in blue triangles and fits as red dashed lines.

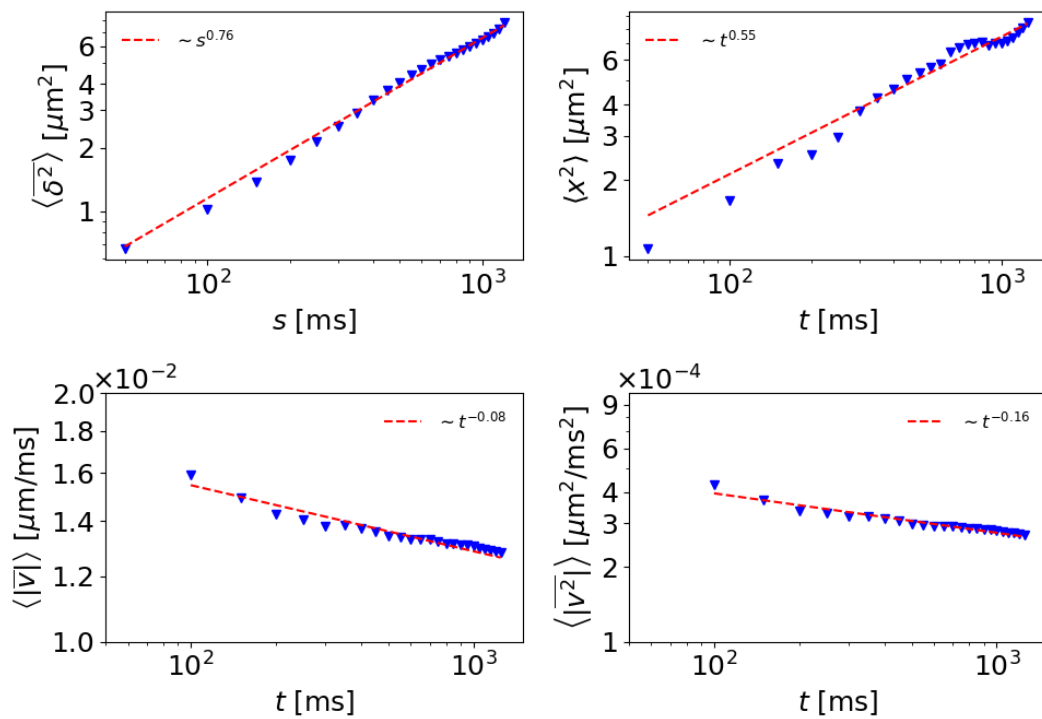


Figure A2: Statistics for fluorescent Rhodamine molecules with relative humidity of 90%. All panels were fitted for $50 < t < 1500$ ms. Measured values are plotted in blue triangles and fits as red dashed lines.

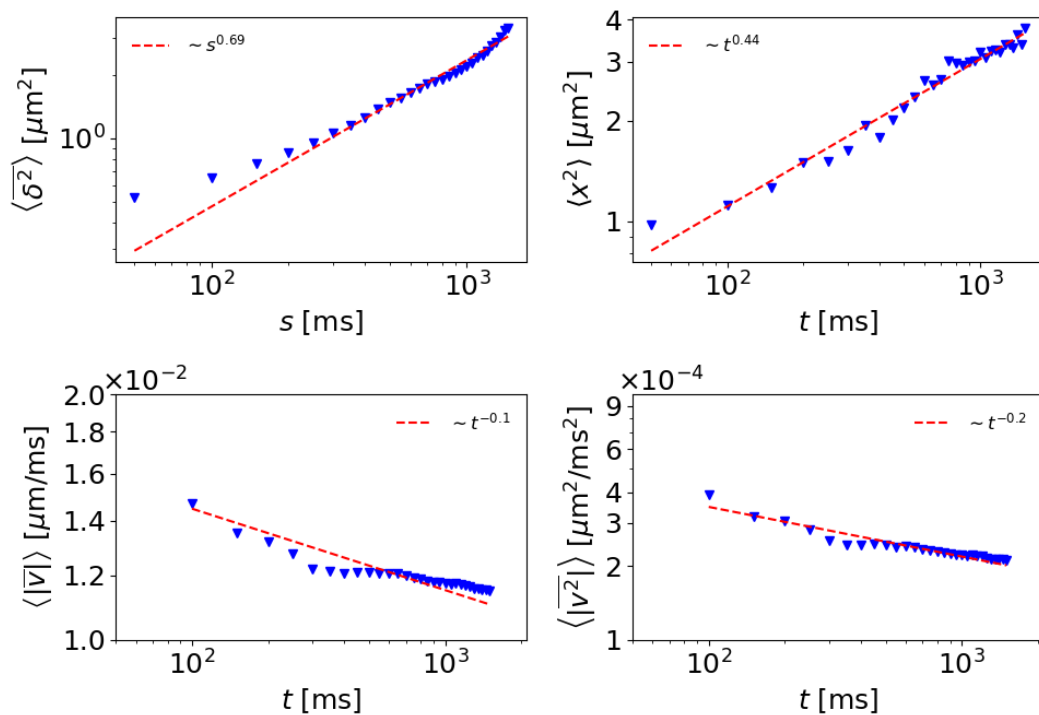


Figure A3: Statistics for fluorescent Rhodamine molecules with relative humidity of 85%. All panels were fitted for $50 < t < 1500$ ms. Measured values are plotted in blue triangles and fits as red dashed lines.

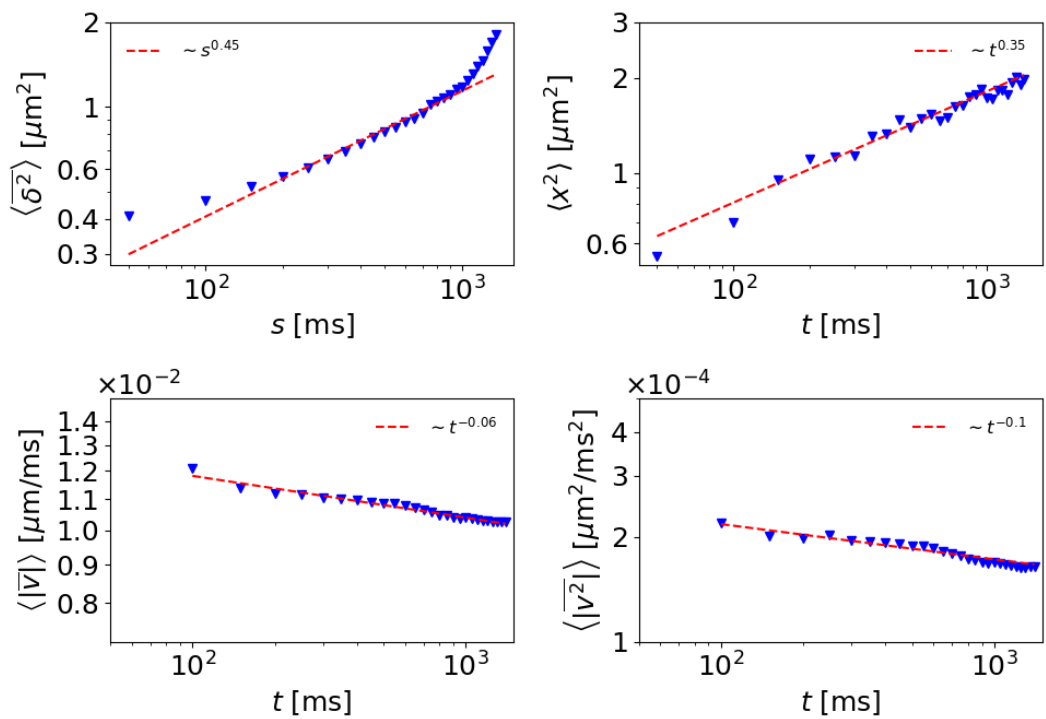


Figure A4: Statistics for fluorescent Rhodamine molecules with relative humidity of 75%. All panels were fitted for $50 < t < 1500$ ms. Measured values are plotted in blue triangles and fits as red dashed lines.

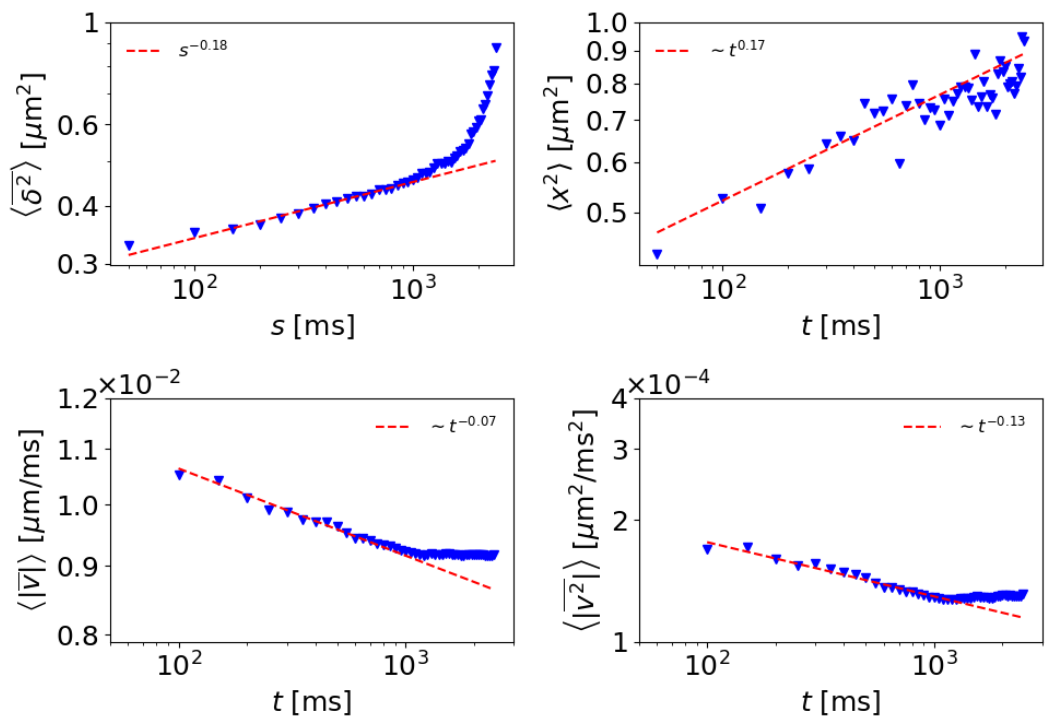


Figure A5: Statistics for fluorescent Rhodamine molecules with relative humidity of 30%. All panels were fitted for $50 < t < 1500$ ms. Measured values are plotted in blue triangles and fits as red dashed lines.

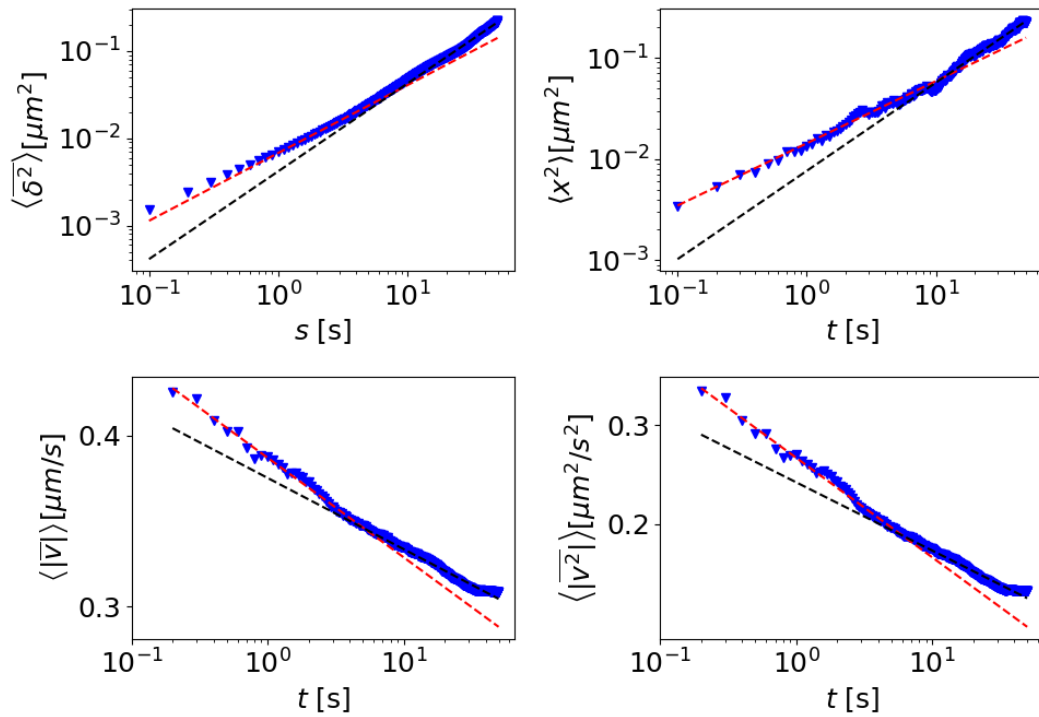


Figure A6: Tracers (quantum dots) in cytoplasm of treated mammalian cells. All panels were fitted in two regimes, $0.1 < t < 5$ s and $5 < t < 50$ s. Measured values are plotted in blue triangles and fits as red and black dashed lines for short and long times respectively.

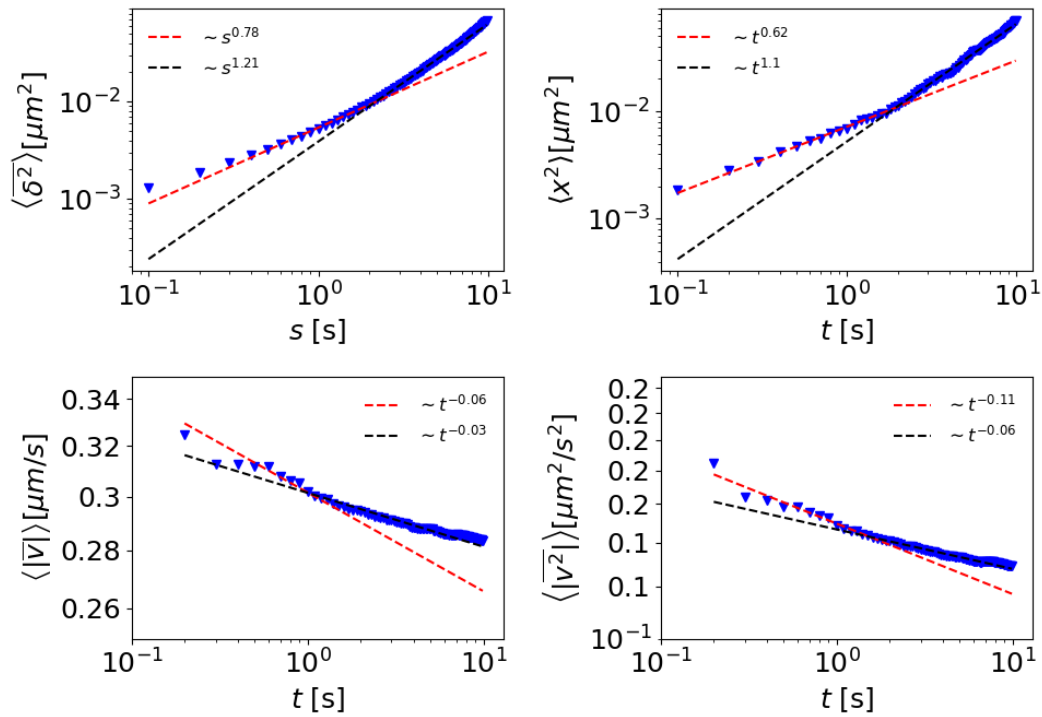


Figure A7: Tracers (quantum dots) in cytoplasm of untreated mammalian cells. All panels were fitted in two regimes, $0.1 < t < 2$ s and $2 < t < 8$ s. Measured values are plotted in blue triangles and fits as red and black dashed lines for short and long times respectively.

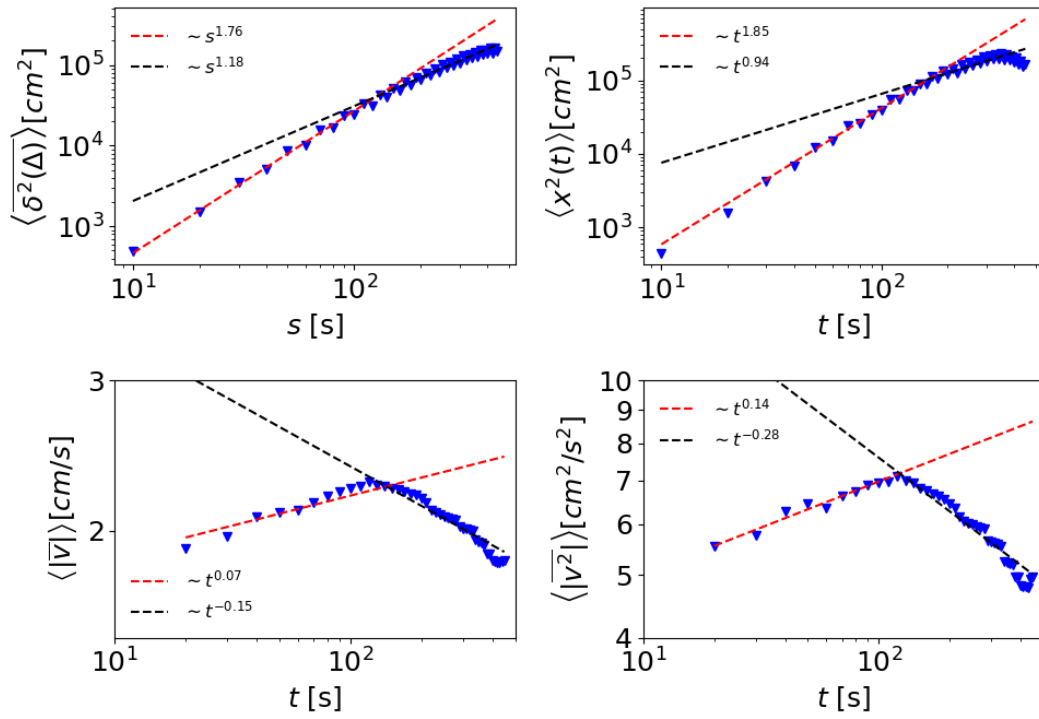


Figure A8: Harvester ants. All panels were fitted in two regimes, $10 < t < 100$ s and $100 < t < 400$ s. Measured values are plotted in blue triangles and fits as red and black dashed lines for short and long times respectively.

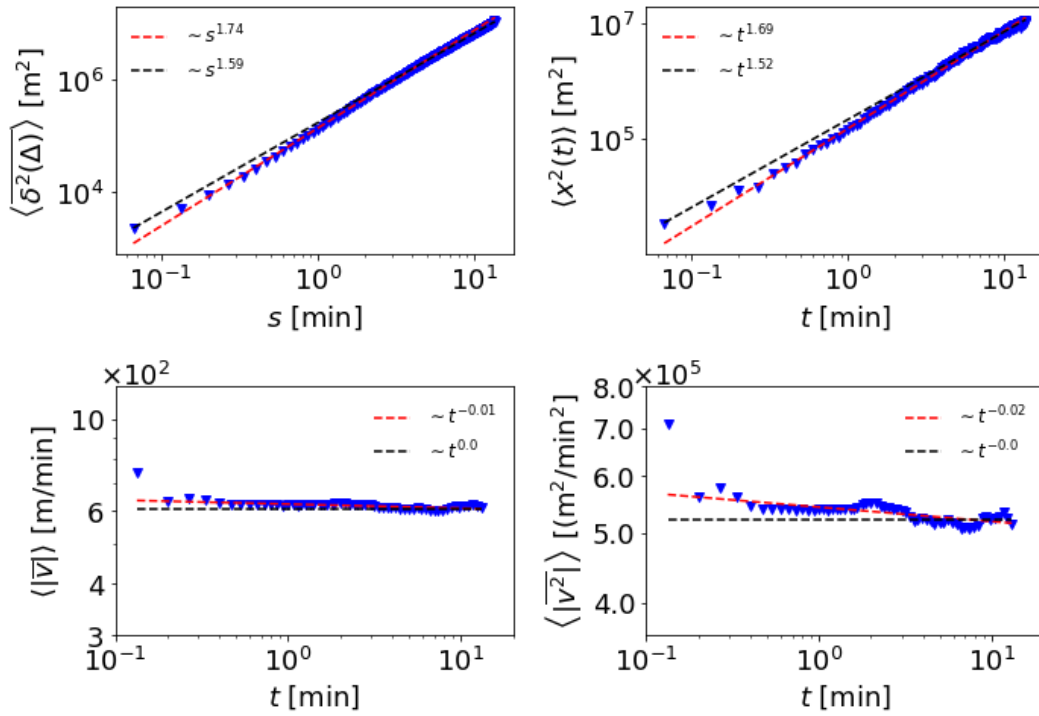


Figure A9: kite - commuting. All panels were fitted in two regimes: $0.1 < t < 3$ and $3 < t < 12$ min. Measured values are plotted in blue triangles and fits as red (short times) and black (long times) dashed lines. Of these trajectories 107 last ≥ 10 min.

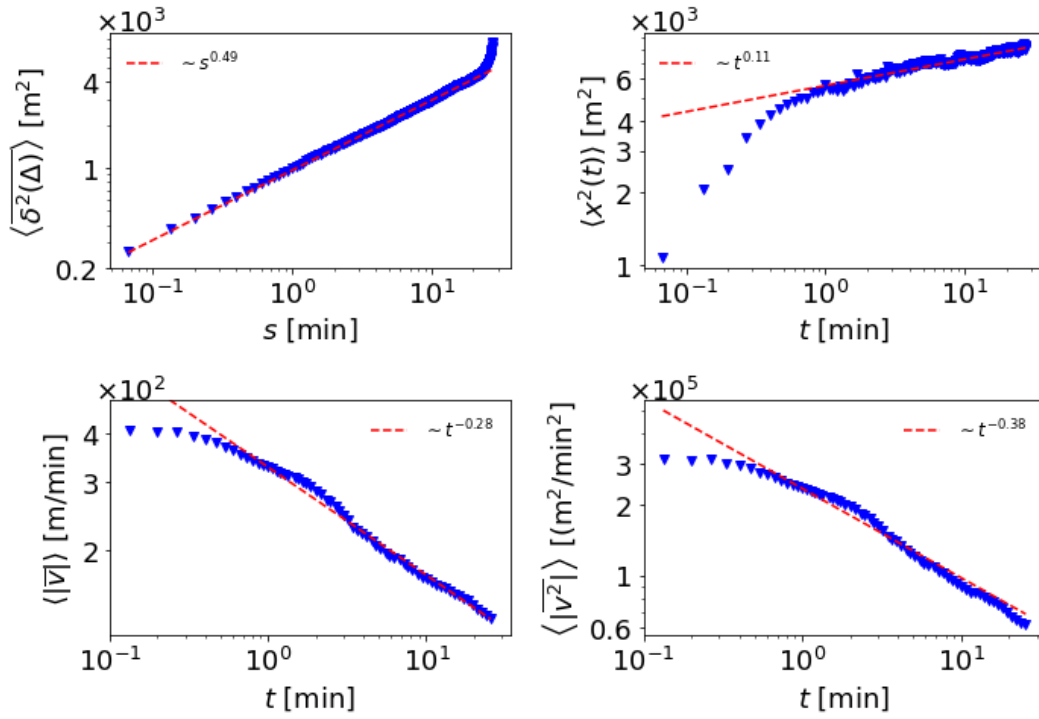


Figure A10: kite searches. All panels were fitted for $0.1 < t < 20$ min. Measured values are plotted in blue triangles and fits as red dashed lines. Of these trajectories 587 last ≥ 27 min.

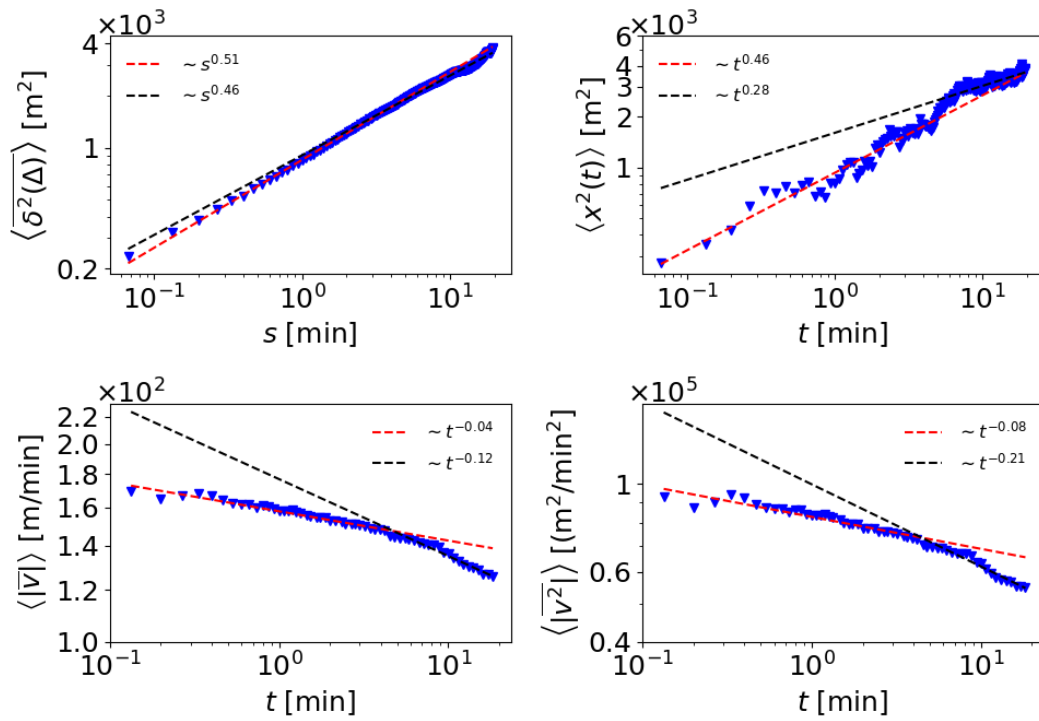


Figure A11: kite searches - aged system. All panels were fitted in two regimes, for $0.1 < t < 5$ min and $5 < t < 20$ min. Measured values are plotted in blue triangles and fits as red dashed lines.

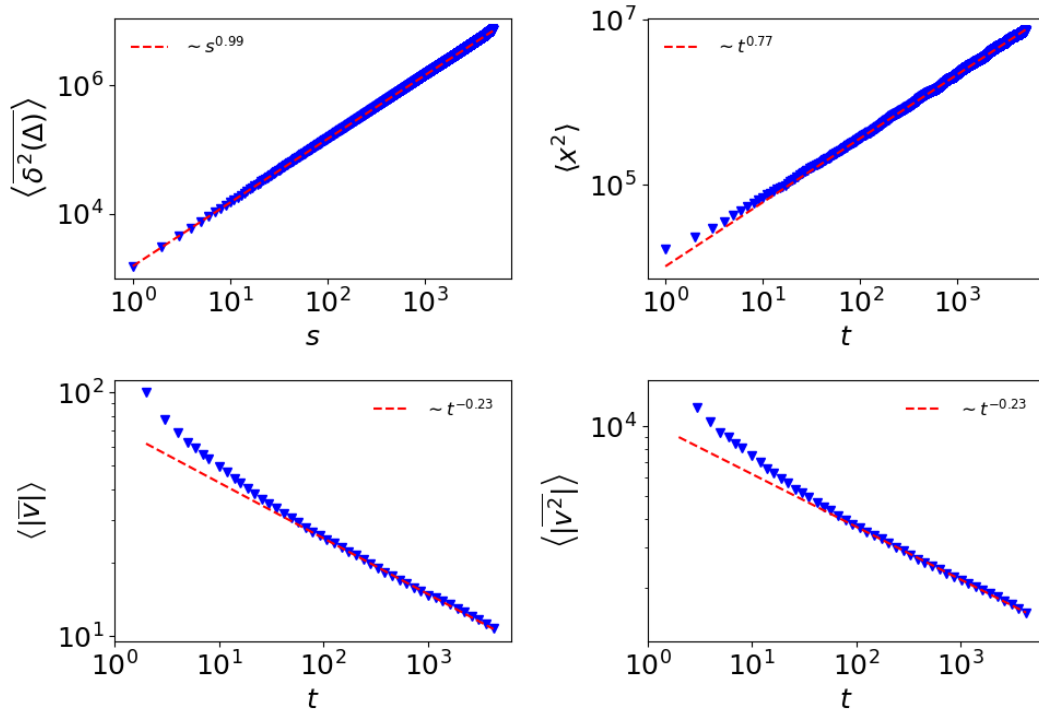


Figure A12: Free CTRW with $\alpha = 0.8$. All panels were fitted for $100 < t < 5000$. Measured values are plotted in blue triangles and fits as dashed lines.